NASS
NAN YANG ACADEMY OF SCIENCES

SUSTAINABLE MARINE STRUCTURES

Volume 4·Issue 1·January 2022 ISSN 2661-3158(Online)

Editorial Board

Editor-in-Chief

Associate Editors

Editorial Board Member

ISSN: 2661-3158 (Online)
Volume 4 Issue 1 January 2022

SUSTAINABLE MARINE STRUCTURES

Editor-in-Chief
Prof. Erkan Oterkus
University of Strathclyde,
United Kingdom

Volume 4 | Issue 1 | January 2022 | Page 1-41
Sustainable Marine Structures

Contents

Articles

Review

Short Communication

Sustainable Marine Structures
https://ojs.nassg.org/index.php/sms

ARTICLE

Thermocline Model for Estimating Argo Sea Surface Temperature

Chunling Zhang[1*] Mengli Zhang[1] Zhenfeng Wang[2] Song Hu[1] Danyang Wang[1] Shenglong Yang[3*]

1. College of Marine Science, Shanghai Ocean University, Shanghai, 201306, China
2. Project Management Office of China National Scientific Seafloor Observatory, Tongji University, Shanghai, 200092, China
3. Key Laboratory of East China Sea & Oceanic Fishery Resources Exploitation and Utilization, Ministry of Agriculture, Shanghai, 200090, China

ARTICLE INFO

Article history
Received: 28 December 2021
Accepted: 4 January 2022
Published Online: 14 January 2022

Keywords:
Argo
Sea surface temperature
Thermocline model
The Pacific Ocean

ABSTRACT

Argo has become an important constituent of the global ocean observation system. However, due to the lack of sea surface measurements from most Argo profiles, the application of Argo data is still limited. In this study, a thermocline model was constructed based on three key thermocline parameters, i.e, thermocline upper depth, the thermocline bottom depth, and thermocline temperature gradient. Following the model, we estimated the sea surface temperature of Argo profiles by providing the relationship between sea surface and subsurface temperature. We tested the effectiveness of our proposed model using statistical analysis and by comparing the sea surface temperature with the results obtained from traditional methods and in situ observations in the Pacific Ocean. The root mean square errors of results obtained from thermocline model were found to be significantly reduced compared to the extrapolation results and satellite retrieved temperature results. The correlation coefficient between the estimation result and in situ observation was 0.967. Argo surface temperature, estimated by the thermocline model, has been theoretically proved to be reliable. Thus, our model generates theoretically feasible data present the mesoscale phenomenon in more detail. Overall, this study compensates for the lack surface observation of Argo, and provides a new tool to establish complete Argo data sets.

*Corresponding Author:
Chunling Zhang,
College of Marine Science, Shanghai Ocean University, Shanghai, 201306, China;
Email: clzhang@shou.edu.cn
Shenglong Yang,
Key Laboratory of East China Sea & Oceanic Fishery Resources Exploitation and Utilization, Ministry of Agriculture, Shanghai, 200090, China;
Email: ysl6782195@126.com

DOI: http://dx.doi.org/10.36956/sms.v4i1.474

1. Introduction

Global Argo array, consisting of more than 3000 profiling floats, has become an important constituent of the global ocean observation system. They are configured and pumped to ensure the highest quality data acquisition from global ocean. To avoid the degradation of salinity accuracy owing to sea surface contaminants, the pump is turned off at ~5 dbar beneath the sea surface as the Argo float ascends. Therefore, the conventional Argo floats obtain temperature and salinity measurements from depths of ~5- 2000 m. Although sea surface temperature (SST) is the key indicator of climate change, it is integral for both ocean circulation and climate change studies [1]. The combination of Argo and satellite SST has been used in several studies [2-4], even though neither the spatial nor the temporal resolution of the two data sets are similar.

A SST salinity (STS) sensor, developed by Sea-Bird Electronics Inc., was used on the Argo float and in the Aquarius Sea Surface Salinity Mission, to measure SST and salinity. This sensor can be used in conjunction with the main SBE-41 CP CTD installed in an Argo float [5]. The STS sensor samples at 1 Hz concurrently with the SBE-41 CP CTD near the float park depth (960- 980 dbar) and subsequently in the upper ocean (3- 20 dbar) just before the SBE-41 CP is turned off. With the increasing demands of such new Argo floats, a large number of near-surface temperature and salinity data are expected to be generated for ocean and atmospheric research. However, the stability of the new Argo floats with STS sensor still needs to be significantly improved. The STS sensor were first put into use in October, 2008; however, by the end of 2020, the number of STS sensors launched by international Argo plan member countries was still <1000. At present, near-surface temperature and salinity data are significantly lesser compared to that required for climate prediction and data assimilation. Therefore, it is necessary to use statistical methods to estimate SST with the help of Argo subsurface data.

It is necessary to assimilate Argo alone or in combination with other observations to generate gridded dataset with the aid of data assimilation techniques, which can be directly used for studies [6]. Due to the lack of surface measurements, some Argo gridded dataset considers 5 m (the nearest surface observation depth of traditional Argo float) as the first surface layer without using additional data [7,8]. Most of Argo datasets consider satellite SST or the added surface measurement data obtained from observation stations as the surface data [9-12]. Roemmich and Gilson obtained Argo observations at ~0–2000 m by linear interpolation and generated climate data for 58 vertical depths [13]. Some other scholars used satellite SST directly, for determining surface temperature of Argo dataset or adopted Akima's extrapolation method to obtain SST [14,15].

The increasing volume of in situ observations are far behind that of Argo. Moreover, in situ data cannot match the increasing volume and temporal length of Argo observations in the near future. In the past few decades, the satellite derived SST has become a primary data source owing to its global spatial coverage and high temporal resolution, however, it is not based on in situ measurements. The retrieved satellite data is significantly different from SST measured in situ at depths of ~0.2- 2 m [16]. The simple combination of satellite SST and Argo subsurface data produces large errors [17]. Several studies employ widely used extrapolation techniques, which are simple method and provide a rough estimation of temperature and salinity. To avoid these short-comings, we propose a parametric model based on thermocline parameters. The SST in the Pacific Ocean was estimated using the subsurface Argo data to verify the accuracy of this model. The Argo observations and the principle of the used method are described in Section 2. In Section 3, we verify our results, and apply them to discuss the thermocline and vertical temperature structure in section 4. Finally, in section 5, we present our conclusions.

2. Materials and Methods

2.1 Data Processing

Three types of marine data are open-accessed for worldwide research, including Argo subsurface profiles, Global Temperature and Salinity Profile Project (GTSPP) data, and Argo Near-surface Temperature (Argo NST). The traditional Argo profiles used to calculate the model parameters were provided by China Argo Real-time Data Center (ftp://ftp.argo.org.cn/pub/ARGO/global/). Due to the dependence of our proposed methods on thermocline parameters, test data that reflect notable thermocline characters are required. Considering the number of Argo observations, data from August, 2020 was chosen as the test data. The test data consisted of a total of 12,726 profiles measured during August, 2020 in the Pacific Ocean (Figure 1a). The data passed a series of quality control tests, such as the test of observation parameters and layers, land, ocean and region detection, density inversion test, the test of range of temperature and salinity, and time judgment [18]. Meanwhile, the estimated SST from Argo subsurface data depended on the initial depth as different reference layers provided different results. These results were weighted by comparing with GTSPP sea surface observations obtained from buoy stations at

depths of ~0.2- 2 m. The GTSPP profiles are obtained from National Oceanic and Atmospheric Administration (NOAA) (http://data.nodc.noaa.gov/gtspp/best.nc/). After removing duplicate data, a total of 6230 profiles during August, 2020, which were mostly located in the equatorial Pacific region was obtained (Figure 1b).

Argo NST observation was used to verify the results estimated from our proposed model. Argo NST data of the same period are available on the National Oceanography Centre's (NOC) ftp website (ftp://ftp.pol.ac.uk/pub/bodc/argo/NST/). These floats with non-pumped near-surface temperatures are deployed and processed by the British Oceanographic Data Centre, the Indian National Centre for Ocean Information Services, the Japan Meteorological Agency, the Scripps Institution of Oceanography, and the University of Washington, respectively. Collectively, a total number of 540 profiles were used in this study, and most of them were primarily located in the western part of the Pacific Ocean (Figure 1b).

2.2 Thermocline Model

The model proposed in this study estimates the SST base at the mixed layer depth (MLD) or the thermocline upper depth, the thermocline bottom depth (TBD), and thermocline temperature gradient (TTG). These key parameters were calculated by the maximum angle method [19-21]. The proposed model was improved and a new application in estimating Argo surface temperature. We constructed the model depicted in Equation (1) by considering the minimal possible degrees of freedom. Figure 2 illustrates the principle behind the proposed model. The estimated SST of Argo from subsurface temperature was different for different reference layers. In this study, 10 m, 20 m, 30 m, 50 m, 75 m, 100 m, 125 m, 150 m, and 200 m were chosen as reference layers to estimate SST in the Pacific Ocean. Subsequently, nine different temperatures measured at each grid were averaged according to (Equation 2):

$$\begin{aligned} SST &= \frac{P_0}{P_z} T_z, \qquad (0 \le z \le \mathrm{MLD}) \\ SST &= T_z - \mathrm{TTG}(z - \mathrm{MLD}), \quad (\mathrm{MLD} \le z \le \mathrm{TBD}) \end{aligned} \tag{1}$$

$$SST_i = \frac{\sum_{j=1}^{9} b_{i,j} SST_{i,j}}{\sum_{j=1}^{9} b_{i,j}}, \qquad b_{i,j} = \exp(-(r_{i,j} - \bar{r}_i)^2 / L^2) \tag{2}$$

where SST is sea surface temperature. Tz is the subsurface temperature at the depth of z estimated by Argo temperature profile data. The parameters P0 and Pz represent sea surface and subsurface pressure, respectively. To ensure the continuity of Tz and Tz' (the differential of Tz) at TBD, the temperature function at depth below the TBD was adopted as gauss function $T_z - T_d = (T_{td} - T_d)\exp[\frac{z_0^w - (z_0 + z + \mathrm{TBD})^w}{H^w}], (z \ge \mathrm{TBD})$, similar to that used in previous work [19]. H^W is the depth scale and Ttd is the temperature at TBD obtained by dichotomy. Td is the temperature in the deepest layer. Base on continuity T(TBD+0)=T(TBD-0) and $\frac{dT(\mathrm{TBD}+0)}{dz} = \frac{dT(\mathrm{TBD}-0)}{dz} = \mathrm{TTG}$, differentiation of the gauss function with respect to z is $z_0 = [\frac{HG_{th}}{w(T_{th} - T_d)}]^{1/(w-1)}$.

The w parameter should be less than 1, otherwise, z_0 becomes significantly large, and temperature starts decreasing with depth. Table 1 shows the root mean square errors (RMSEs) of the estimated results with different W and *H*. When W is constant, the RMSE values decrease initially, and subsequently increases. The RMSE values are least value when *H*=2000 m. Moreover, *H* is constant

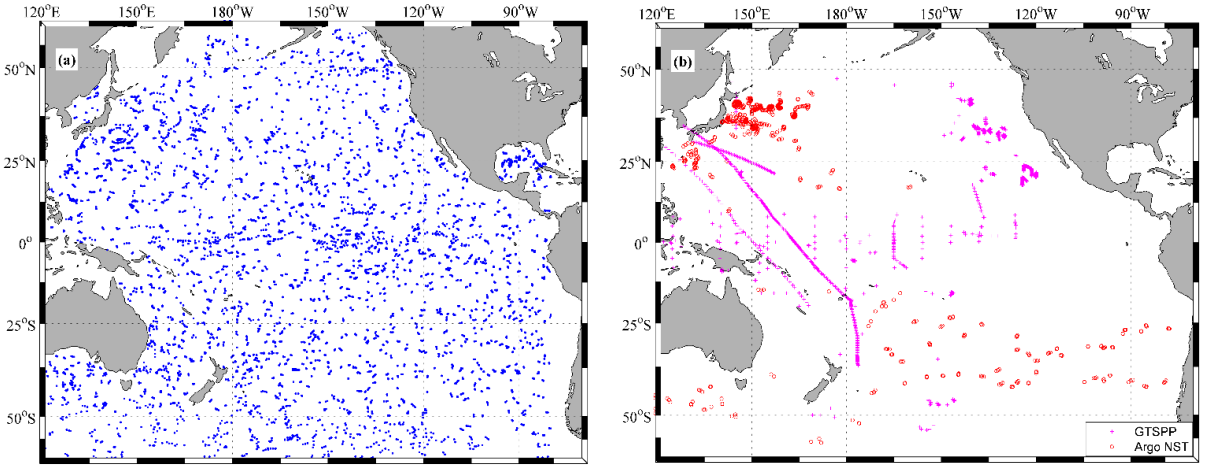

Figure 1. Locations of Argo subsurface profiles (a), and (b) GTSSPP or Argo near surface observations.

and the RMSEs of the estimated temperatures are the least when W=0.5. Hence, W and *H* were set as 0.5 and 2000 m, respectively, to ensure the least RMSE at a temperature of 0.637 °C. SSTi is the estimated SST at the i th section of the Argo profile. SSTi,j is the estimated temperature at ith profile according to jth (j=1,2,…9) datum layer. rij is the RMSE for SSTi, j and GTSPP data. The different results at different starting depth have minimum temperature RMSE compared with GTSPP when the correlation scale *L* has a value of 2 degrees (Figure 3).

2.3 Algorithm of Thermocline Parameters

To estimate the SST by Equations (1) and (2) described in section 2.2, the key parameters—MLD, TBD, TTG should be determined. The maximum angle method [20,21], a simple and objective method, was adopted to calculate these parameters with the Argo dataset of August, 2020. It not only uses the main feature (vertically uniform) of the mixed layer (i.e., temperature (or density) deviation and vertical gradient criteria) but also uses the main characteristics of the thermocline (sharp gradient) beneath the mixed layer. However, this method can be improved, when the variable is strictly monotonous, the depth of density mixed layer is regarded as isothermal layer depth.

To ensure a monotonous profile, the maximum angle method of the potential density profile was used to determine thermocline parameters via Argo observations. Figure 4 illustrates the methodology used by a potential density profile. The vertical density difference represents the total variability of potential density. Theoretically, the variability of the vertical density difference is approximately zero in the constant-density layer, and it becomes larger in the pycnocline beneath the mixed layer. It is reasonable to identify the main parts of the pycnocline between the two depths. The main depths were set corresponding to 10% and 70% difference in vertical density. The MLD and TBD were determined between the main depths by point to point linear polynomial fitting. Figure 4 provides a schematic representation of the vector fitting used in our proposed method. At depth z_k (marked by a circle in Figure 4), both vectors (downward positive) were constructed by linear polynomial fitting of the profile data from z_{k-1} to z_k. The subscript k increases downward with k = 1 at the surface or at the nearest location to the surface. In the constant-density (isothermal) layer, the angle θ reaches its maximum value (see Figure 4b), and is smaller if z_k is inside (Figure 4a) or outside (Figure 4c) the

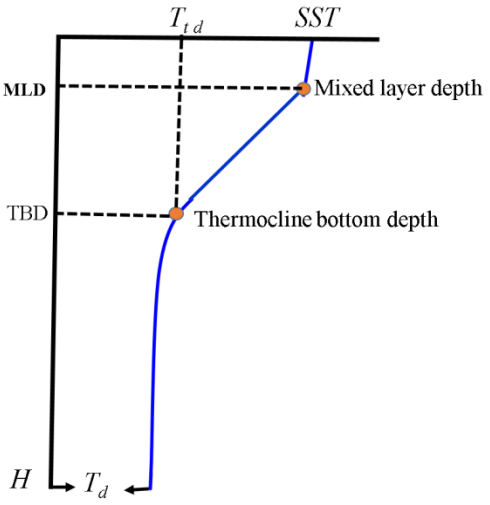

Figure 2. Principle of thermocline parametric model. SST denotes sea surface temperature. The parameters h1, h2 and H represent mixed layer depth, thermocline bottom depth, and depth scale, respectively.

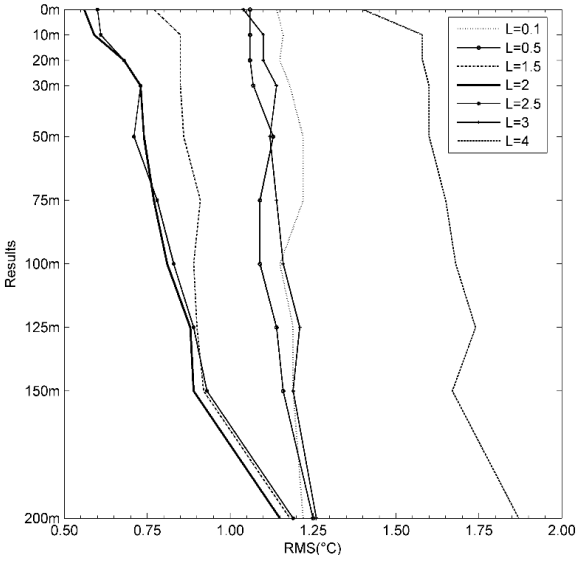

Figure 3. Different RMSEs of SST (°C) for different correlation scale L.

Table 1. Estimated RMSEs of SST (°C) with different *W* and *H* values

	$W = 0.1$	$W = 0.25$	$W = 0.5$	$W = 0.6$	$W = 0.8$
***H*=1000 m**	1.123	0.971	0.805	0.812	0.877
***H*=1500 m**	0.908	0. 884	0.795	0.819	0.830
***H*=2000 m**	0.782	0.761	**0.637**	0.800	0.802
***H*=3000 m**	0.851	0.780	0.711	0.873	0.935
***H*=5500 m**	0.893	0.852	0.790	0. 963	1.020

mixed layer. Thus, the maximum angle principle can be used to determine the mixed layer depth (θmax, $MLDz_k$). In practice, the angle θ is difficult to calculate, therefore, tan θ was used instead.

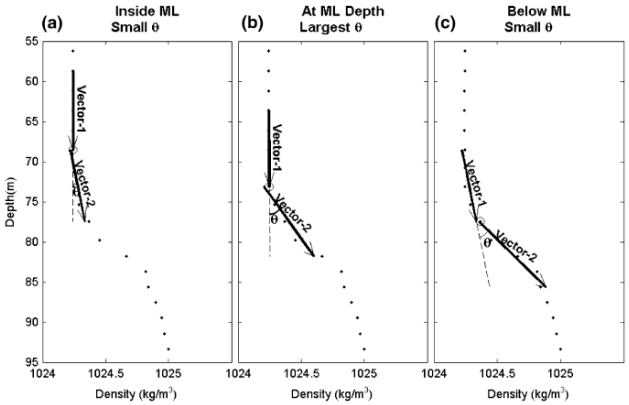

Figure 4. Illustration of the max angle method. The dots represent density of each depth. The vector angles (indicated by θ) have small value inside or outside the mixed layer depth ((a) and (c)), and it has the largest value at the depth of thermocline upper depth.

In order to ensure the stability of the simulation results from the sbPOM model, the time of the outer mode (positive compression mold) was set to 20 s and the time of the inner mode (oblique compression mold) was set to 600 s. The bathymetric topography was based on the General Bathymetry Chart of the Oceans (GEBCO), which has a minimum water depth of 10 m. The maximum water depth was set to 5000 m, and water depths exceeding 5000 m were replaced by 5000 m to match the maximum water depth in the SODA data. The spatial resolution of the simulated sea surface temperature from the sbPOM model is a 0.25° grid at a 1-hour interval.

3. Validation of the Results

3.1 Correlation Analysis

The estimation of SST from subsurface temperature using the thermal parametric model (Figure 2) is based on the hypothesis proposed by Chu and Fan [20]. The linear correlation coefficient between SST anomaly and MLD anomaly is significantly larger than that between SST anomaly and other parameters, i.e., $|r_1|>|r_2|$, $|r_1|>|r_3|$in formula $MLD'=r_1SST'$, $TBD'=r_2SST'$, $TTG'=r_3SST'$ where, r_1, r_2, r_3 are the regression coefficients of MLD', TBD', TTG', respectively. The parameter anomalies (SST', MLD', TBD', TTG') were obtained from the thermal parameters (SST, MLD, TBD, TTG) by subtracting their mean values within a 1o×1o grid cell at each observation locations.

Figure 5 shows the scatter plot between SST' and (MLD', TBD', TTG') in the Pacific Ocean. The data points concentrate around the fitting line in Figure 5a. Although the data points in Figure 5b and 5c plot relatively far away from the fitting line, three absolute values of r obtained by linear regression indicate that MLD' has the largest correlation coefficient with SST' among all subsurface parameters. The correlation coefficients between SST' and MLD', TBD', and TTG' were 0.249, −0.046, and 8.334e-04, respectively. The significance of the correlation was evaluated by statistical analyses $t=\frac{r\sqrt{n-2}}{\sqrt{1-r^2}}$, where the t distribution had a degree of freedom of n-2. Here, r is the correlation coefficient and n is the number of analyzed samples (19,200). The critical value of t at significance level of 0.005 was 2.576 ($t_{0.005}$ (19200-2)=2.576). Three absolute values of t between SST' and MLD', TBD', and TTG' were 1.832, –0.326, and 0.059, respectively. These values were less than the critical value of 2.576. In other words, we can suggest that the analyzed data are within the uncertainty of the statistical test.

From the above analysis, we conclude that the correlation coefficient between the two short timescale parameters SST' and MLD' is significantly larger than that between SST' and the long timescale parameters (TBD', TTG'). This in turn theoretically confirmed the reliability of estimating SST based on thermal parametric model in the Pacific Ocean.

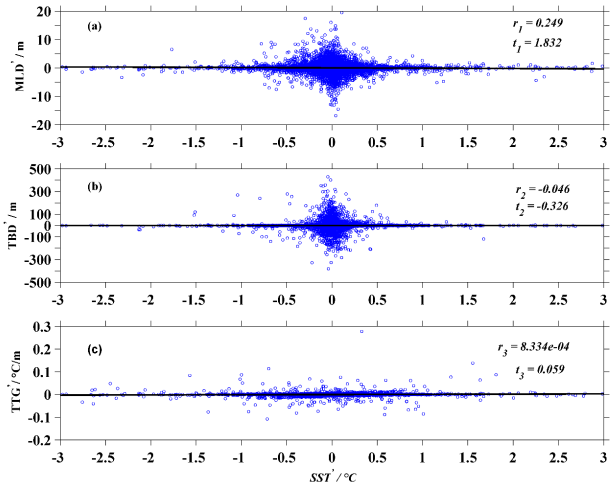

Figure 5. Correlation analysis between sea surface temperature anomaly and thermocline parameter anomaly. (a) The correlation coefficients between sea surface temperature anomaly and mixed layer depth anomaly, (b) thermocline bottom depth anomaly, and (c) thermocline gradient are represented by r1, r2, and r3, respectively. The parameter t indicates t-critical at significance level of 0.005.

3.2 Comparison with Observations

The commonly used methods to obtain Argo surface temperature include extrapolation method proposed by Akima [22] and satellite derived SST. According to the thermocline model (described in 2.2), the estimation of SST was based on reference layers (10 m, 20 m, 30 m, 50 m, 75 m, 100 m, 125 m, 150 m, 200 m) and different results were weighted by gauss function. Next, we compared the temperature results from the different datum layers, the thermocline model (recorded as SST), Akima extrapolation (named as extra), and satellite AMSR-E SST (indicated by satellite) by considering the data obtained from GTSPP and Argo NST observations as true values.

Table 2 lists the RMSEs of temperature estimated from the nine different datums, weight-averaged SST based on Equation (2), the surface temperature obtained by extrapolation (extra) and satellite AMSR-E SST (satellite) compared with GTSPP and Argo NST. It is evinced that the temperature RMSEs increase with the datum depth in the results obtained from thermocline model. The weighed-averaged SST has smaller RMSE of 1.04 °C and 0.99 °C compared to that of GTSPP and Argo NST, respectively. However, the RMSEs of estimated temperatures corresponding to the nine datum layers were all less than 1.6 °C for the two base datasets. The RMSEs between the extra surface temperature and the two practical datasets have a value of >1.8 °C, which are larger than all estimations. The RMSEs between the satellite AMSR-E SST and the two practical datasets are ~2 °C and 1.5 °C relative to GTSPP and Argo NST, respectively. Although both GTSPP and Argo NST are sparse and asymmetrical in space, Table 2 illustrates that the SST estimated by thermocline parametric model is more close to in situ observation compared to satellite and extra. Meanwhile it indicates that weighted mean method (formula (2)) can improve the accuracy of estimation. Moreover, the in situ Argo NST and GTSPP data were not used during the estimation process, as discussed below. Thus, the test was strictly independent.

The correlation analysis results and absolute temperature errors of SST derived from thermocline model SST (Figure 6a), extrapolated results (indicated by extra in Figure 5b), and satellite derived (Figure 6 c) are displayed in Figure 6. Figures 6(a1), (b1), and (c1) provide the correlation coefficient R, RMSE, regression line, and its confidence interval with confidence level of 90%. It is evident that SST in the Pacific Ocean is in better agreement with Argo NST compared to extra or satellite. The SST data points concentrate around the fitting line $y = 0.99x + 1.05$, and have the smallest residual standard deviation (S = 1.72) compared to other methods. The correlation coefficient between SST and Argo NST was 0.967, which is smaller than the other results. The distribution of extra and satellite data points are more dispersed, with linear fitting coefficients of 0.87 and 0.89, respectively. Both extra and satellite derived results have high correlation with the Argo NST with correlation coefficients of 0.911 and 0.937, respectively. However, their RMSEs were significantly larger than that of SST. The maximum absolute temperature errors of thermocline model shown in Figure 5 a2 are <1 °C. In fact, most of the errors in the estimated temperature were <0.5 °C. There are a few profiles near 40 °N with temperature errors of ~ 1 °C. Most of the errors in temperature estimated by extrapolation and satellite based were >1.5 °C, with the maximum error exceeding 2.5 °C in the Northwest Pacific.

Argo NST data shown in Figure 6 are sparse in the equatorial region. The GTSPP observations were primarily obtained from the anchor buoys in tropical Pacific. Figure 7 shows the absolute temperature errors between the different results and GTSPP in the equatorial Pacific. The temperature errors of SST obtained from the thermocline model (Figure 7a) were minor at all observation locations. Most of the SST errors were <0.5 °C with a few temperature errors being in the range of 0.5- 1.0 °C. In contrast, the errors in temperature of extra and satellite displayed a skewed distribution, especially in the extrapolation results (Figure 7b). Most of these errors in extra temperature exceed 1.5 °C and half of the total errors were approximately at 2.5 °C. In the satellite results (Figure 7 b), the errors in temperature were concentrated at 0.5–2.0 °C, which are smaller than that obtained in the extra results but larger than in the thermocline model SST errors. Thus, both theoretical statistics and observation comparisons show that the thermocline model can provide more accurate results.

4. Discussion

4.1 Thermocline Parameters Analysis

Three thermocline parameters involved in this study

Table 2. RMSEs of the estimated temperature (°C) for different SST and in situ observation

Results	10m	20m	30m	50m	75m	100m	125m	150m	200m	SST	Extra	Satellite
GTSPP	1.13	1.15	1.18	1.10	1.20	1.52	1.59	1.44	1.51	1.04	1.94	1.96
Argo NST	1.04	1.21	1.21	1.16	1.26	1.28	1.35	1.48	1.54	0.99	1.84	1.50

vary with respect to different timescales. The MLD has a short correlation timescale. On the other hand, the TBD and TTG have longer correlation timescales. The strongest thermocline in the northern hemisphere and the weakest in the southern hemisphere appears during August [23]. This is reflected from the distribution of thermocline parameters of August, 2020 obtained from Argo profiles and gridded by the optimal interpolation [24,25] (Figure 8).

There are more than 60% MLDs lesser than 100 m as obtained by Argo profiles. Most of them are in the Northern Pacific (Figure 8 (a1)). The MLD in the Southern Pacific are concentrated at 100- 300 m. Most of the deeper MLD are located to the south of 40 °S, where there is no noticeable thermocline in August and the vertical temperature variation is not evident. It indicates that the thermocline disappears rapidly in this region. Figure 8 (a2) displays the variation of the mean MLD with latitude. The MLD gradually deepens from 60 °N to 40 °N, and

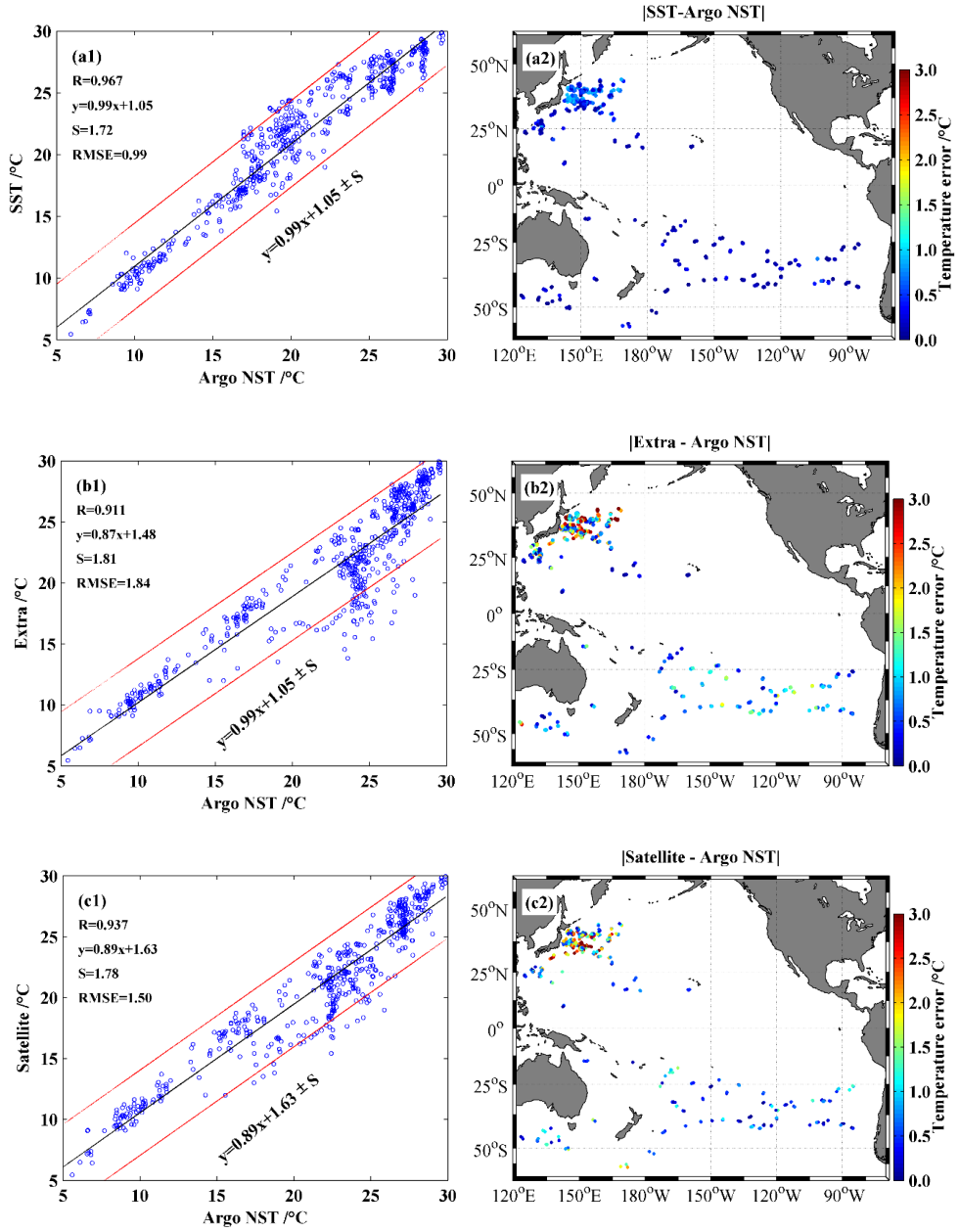

Figure 6. Scatter diagrams of correlation analysis (a1, b1, c1) and absolute temperature errors (a1, a2, a3) between different results and the Argo NST observation. The results of SST obtained using thermocline model, extra obtained by extrapolation, and satellite surface temperature are represented by **(a), (b)**, and **(c)**, respectively. The red lines represent the 95% confidence interval of the regression line (black line) with the residual standard deviation (indicated by S). The correlation coefficient is represented by R.

become shallow in the subarctic. The mean MLD is lower than 50 m in the northern Pacific, and has a value of more than 100 m in the 40 °S–60 °S. These results agree with previous studies [23,26,27]. Thermocline bottom depth is deeper than 100 m, and has higher values in the southern Pacific shown in Figure 8 (c). Its zonal mean value represents increasing trend from north to south similar to the MLD. During August, the thermocline is evident in the northern Pacific. The corresponding TBD is also shallow with a mean value of <200 m. The southern Pacific is characterized by a deeper TBD with a zonal mean value of 300-500 m, and it is even deeper than 800 m at approximately 45 °S. On the other hand, the TBD is ~300 m in the equatorial Pacific.

Temperature gradient represents the strength of the thermocline. Figure 8 (b) illustrates the distribution of TTG and its zonal average. TTG varies from 0 to 0.15 °C/m. TTG is higher than 0.09 °C/m in the tropical Pacific region of 10 °S–10 °N (Figure 8 (b1)). Compared to southern Pacific, the TTG is stronger in most of the northern Pacific region, especially in the regions between 45 °N and 25 °N, where the TTG is generally higher than 0.06 °C/m. The mean TTGs of the northern Pacific are higher than 0.06 °C/m with a value of 0.15 °C/m at approximately 10 °N, as shown in its zonal mean distribution (Figure 8 (b2)). On the other hand, the southern Pacific has a mean TTG of <0.05 °C/m, and the thermocline is notably weakened in the southern hemisphere. TTG is almost close to zero at south of 40 °S, where there is no apparent thermocline.

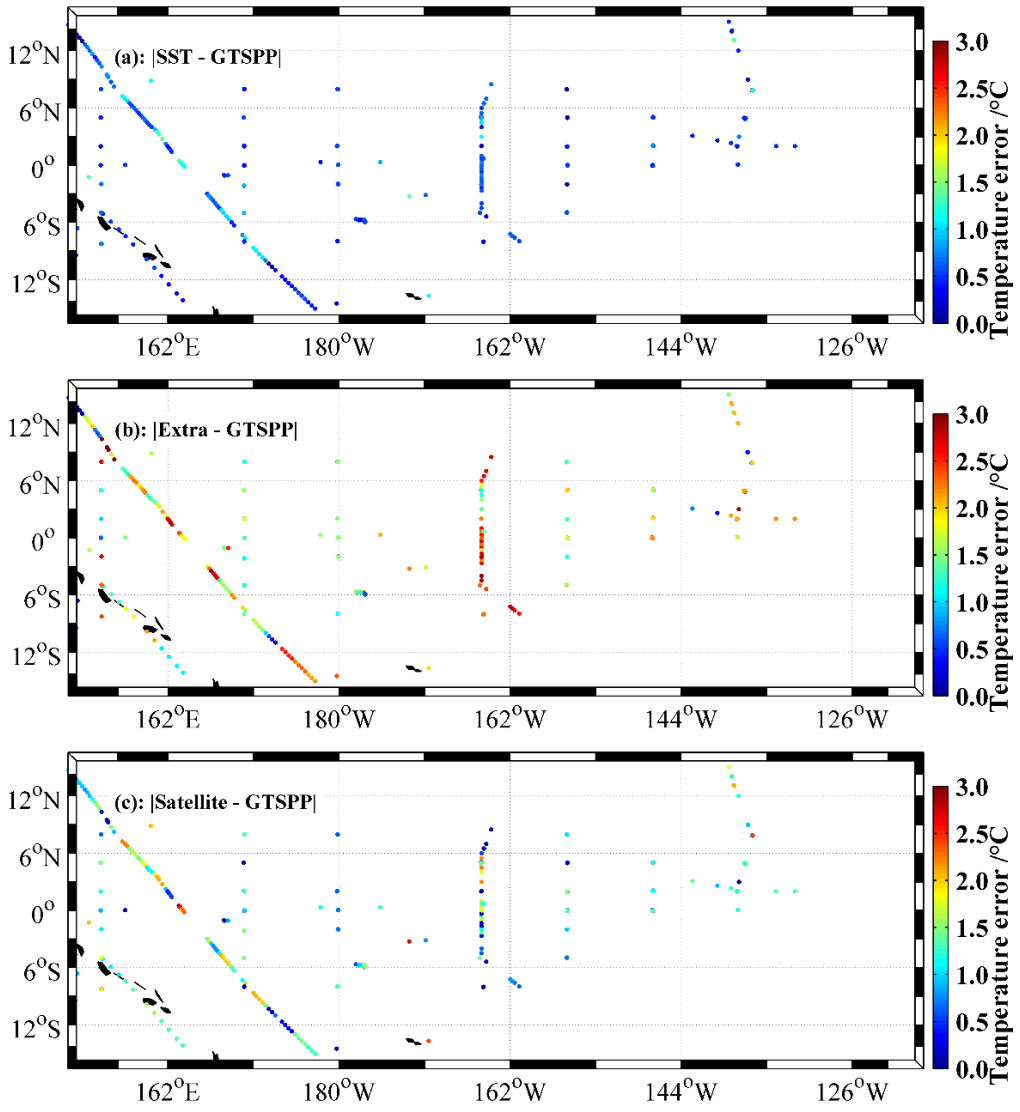

Figure 7. Scatter of absolute temperature errors between thermocline model **(a),** extrapolation **(b)**, and satellite surface temperature **(c)** and GTSPP data.

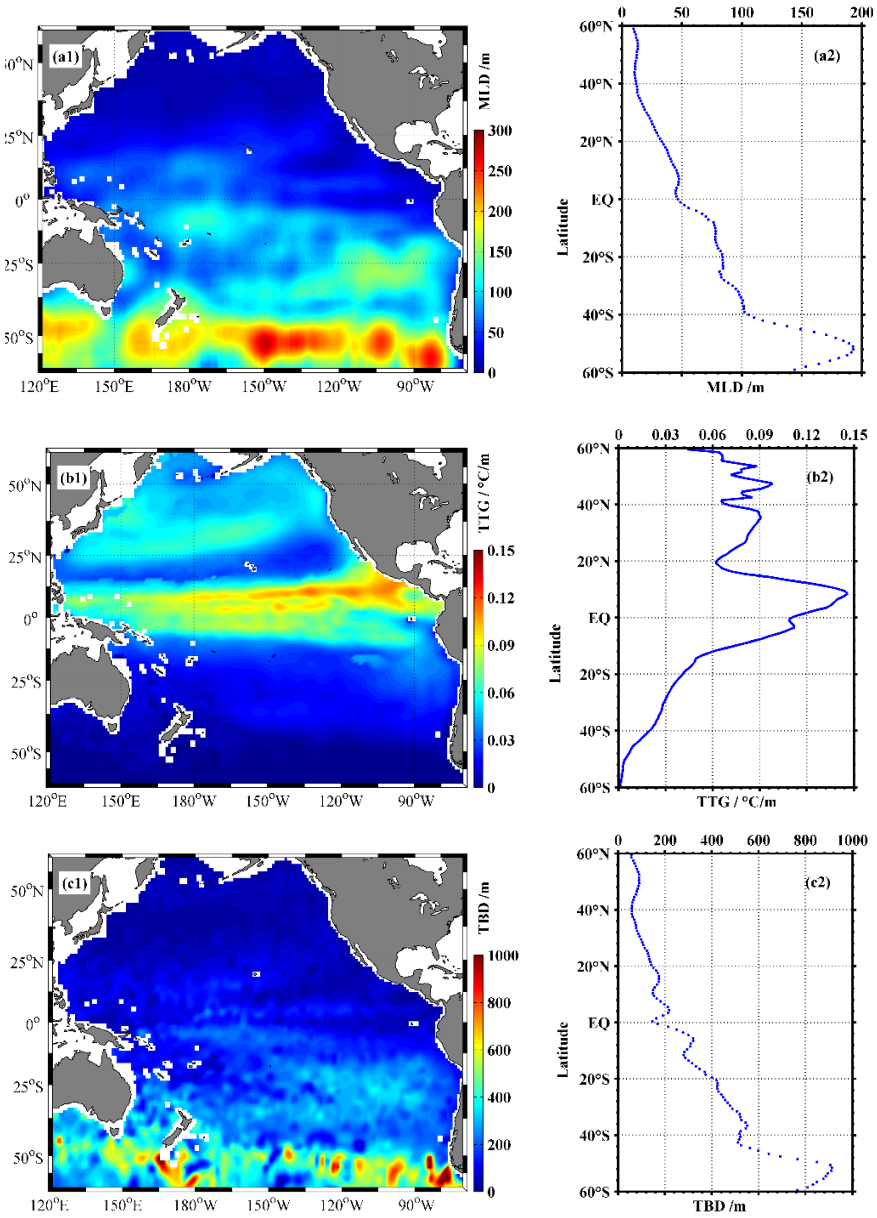

Figure 8. Spatial distribution (a1, b1, c1) and latitude mean (a2, b2, c2) of mixed layer depth **(a)**, thermocline temperature gradient **(b)**, and thermocline bottom depth **(c)**.

4.2 Distribution of Sea Surface Temperature

The thermocline parameter model in section 2.2 provides the monthly distribution of SST. As shown in Figure 9, the surface temperature distribution in the Pacific Ocean shows a trend of increasing temperature in the equatorial region (> 25 °C) and decreasing temperature in the high latitude region. The temperature generally drops below 10 °C in the sub Antarctic and sub polar regions. This reflects the change of solar radiation with latitude. The isotherms are sparse in the range of 20 °S- 20 °N. With temperature transition from the tropics to the polar regions, the isotherms become gradually denser. The isotherms reflect the characters of the polar front at approximately 40 °latitudes. The eastern isotherm between 40 °S and 40 °N bends to low latitudes under the influence of cold current. On the other hand, the western isotherm bends to high latitudes under the influence of warm current. To the south of 40 °S, the isotherm is almost parallel to the latitude. There exists evident warm pool in the equatorial region of the Western Pacific. The center of the warm pool (29 °C isotherm) lies between 5 °S–25 °N during August. These characteristics are consistent with the results obtained from historical observation data and have the potential to extract mesoscale information completely.

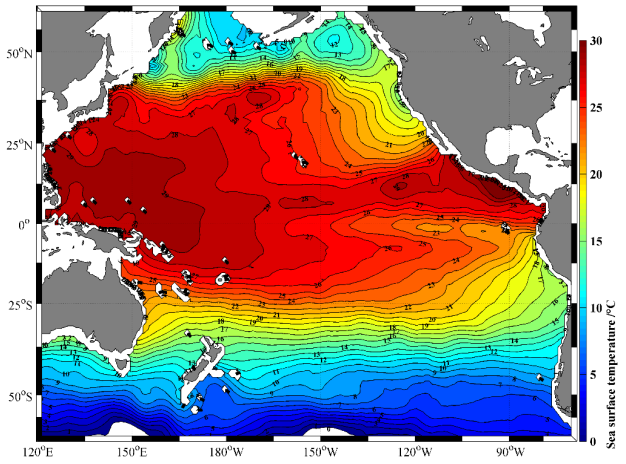

Figure 9. Distribution of the sea surface temperature during August, 2020 in the Pacific Ocean.

5. Conclusions

As one of the important constituents of the global ocean observation system, Argo floats collect temperature and salinity data of upper global ocean rapidly, accurately, and extensively. Argo profiles are increasing at the rate of one hundred thousand sections each year. Meanwhile, SST is an important parameter for both ocean circulation and climate change studies, and several studies rely on complete three-dimension temperature information. Therefore, estimating the Argo SST using available statistic methods has major practical and scientific significance. Based on a thermocline parametric model, the maximum angle method has been used in this study to calculate the model parameters (MLD, TTG and TBD), and subsequently, SST was estimated using Argo subsurface temperature. The estimated results were compared with near surface temperature observations, and were theoretically tested using correlation analysis. The results illustrate that the estimated SSTW is reliable and credible.

In this paper, the maximum angle method was adopted to determine the model parameters (MLD, TTG and TBD). This method is novel, and has stronger theoretical foundation compared to previous methods (e.g. gradient criterion and curvature method). The mixed layer depth obtained by this method is realistic. While using the maximum angle method, the analysis variable should be strictly monotonous. Therefore, the density mixed layer was considered as temperature mixed layer depth in this study. Since the barrier layer was ignored, it is expected to generate certain errors in our model. It is possible to reduce such errors by adopting the temperature profile and combining data from other models in the regions with existing barrier layers.

In addition, the thermocline model employed in this study provides the function between SST and subsurface temperature based on the determined parameters MLD, TTG, TBD etc. For this reason, the accuracy of SST estimated using this method is expected to be relatively lower when the thermoclines are not distinct. Further research is required to overcome these shortcomings. Since the Pacific Ocean was considered as an experimental region to verify the effectiveness of this thermocline model, our study provides a new idea for the construction of Argo SST model in global ocean.

Author Contributions

Conceptualization, C.Z. and C.W.; methodology, C.Z., Z.W., and C.W.; validation, M.Z., D.W., and S.H.; formal analysis, C.Z. and C.W.; investigation, C.Z.; resources, C.Z; writing original draft preparation, C.Z. and C.W.; writing—review and editing, Z.W. and S.H.; visualization, M.Z. and D.W.; funding acquisition, C.Z. All authors have read and agreed to the published version of the manuscript.

Funding

This research was funded by the National Nature Foundation nos. 4210060098, the Argo buoy project under Grant D-8006-21-0082, the Foundation of Key Laboratory of ocean fishery development under Grant A1-2006-21-200201, and the Foundation of fishery resources Comprehensive Scientific Surveys in the Northwest Pacific D-8021-21-0109-01.

Data Availability Statement

Three categories of data used to support the results of this study are included in the article. Argo float data were collected and made freely available by the China Argo Real-time Data Center (ftp://ftp.argo.org.cn/pub/ARGO/global/). Argo NST observation data of the same period are available on the National Oceanography Centre's (NOC) ftp website (ftp://ftp.pol.ac.uk/pub/bodc/argo/NST/). The GTSPP profiles are obtained from National Oceanic and Atmospheric Administration (NOAA) (http://data.nodc.noaa.gov/gtspp/best.nc/).

Acknowledgments

We are grateful to the anonymous reviewers for critically going through the manuscript and for providing necessary comments. We also thank Prof. Chu P of Department of Oceanography, Naval Postgraduate School for several beneficial discussions. Xu Jianping

of the Second Institute of Oceanography is thanked for his comments and English revision. We wish to thank the colleagues at the China Argo Real-time Data Center for numerous presentations and informal discussions that led to the successful implementation of the work presented here. We thank Wiley Editing Services (www.wileyauthors.com/eeo/preparation) for editing this manuscript.

References

[1] Jordi, A., Wang, D.P., 2012. Sbpom: a parallel implementation of prince ton ocean model. Environ. Modell. Softw. 38, 59-61.

[2] Donlon, C., Casey, K., Robinson, I., Gentemann, C., Reynolds, R., Barton, I., Arino, O., Stark, J., Rayner, N., LeBorgne, P., Poulter, D., Vazquez-Cuervo, J., Armstrong, E., Beggs, H., Llewellyn-Jones, D., Minnett, P., Merchant, C., Evans, R., 2009. The GODAE high-resolution sea surface temperature pilot project. Oceanography. 22, 34-45.

[3] Guinehut, S.P., Traon Le, P.Y., Larnicol, G., Philipps, S., 2004. Combining Argo and remote-sensing data to estimate the ocean three-dimensional temperature fields - A first approach based on simulated observations. Journal of Marine Systems. 46, 85-98.

[4] Souza, J.M., Boyer Montegut, A.C., Cabanes, C., Klein, P., 2011. Estimation of the Agulhas ring impacts on meridional heat fluxes and transport using ARGO floats and satellite data. Geophysical Research Letters. 38, L21602.

[5] Hobbs, W.R., Willis, J.K., 2012. Mid latitude North Atlantic heat transport: A time series based on satellite and drifter data. Journal of Geophysical Research. 117, C01008.

[6] Larson, N.L., Janzen, C.D., Murphy, D.J., 2008. STS: An instrument for extending ARGO temperature and salinity measurements through the sea surface. Florida: Poster Presentation Ocean Sciences Meeting. 2008, 2-7.

[7] Xu, J.P., Liu, Z.H., 2007. The experiment of China Argo ocean observing array. Beijing: China Meteorological Press. 4-5.

[8] Chang-Xiang, Y., Jiang, Z., Ji-Ping, X., 2010. An ocean reanalysis system for the joining area of Asia and Indian-Pacific Ocean. Atmospheric and Oceanic Science Letters. 3, 81-86.

[9] Zweng, M.M., Reagan, J.R., Antonov, J.I., Locarnini, R.A., Mishonov, A.V., Boyer, T.P., Garcia, H.E., Baranova, O.K., Johnson, D.R., Seidov, D., Biddle, M.M., 2013. World ocean atlas 2013. Salinity. Ed.; S Levitus. Volume 2.

[10] Martin, M.J., Hines, A., Bell, M.J., 2007. Data assimilation in the FOAM operational short-range ocean forecasting system: A description of the scheme and its impact. Quarterly Journal of the Royal Meteorological Society. 133, 981-995.

[11] Hosoda, S., Ohira, T., Nakamura, T., 2008. A monthly mean dataset of global oceanic temperature and salinity derived from Argo float observations. JAMSTEC Report. Research Developments. 8, 47-59.

[12] Gaillard, F., 2010. ISAS-Tool version 5.3: Method and configuration. Laboratoere de Physique de Oceans. UMR6523, 1-12.

[13] Brion, E., Gaillard, F., 2012. ISAS-Tool version 6: User's manual. Report LPO 01-12. 2012, 1-45.

[14] Roemmich, D., Gilson, J., 2009. The 2004-2008 mean and annual cycle of temperature, salinity, and steric height in the global ocean from the Argo Program. Progress in Oceanography. 82, 81-100.

[15] Wang, H.Z., Wang, G.H., Zhang, R., A., Y.Z., Jin, B.G., 2010. User's Manual of User's Manual of Argo Gridded Salinity Product (G-Argo). Hangzhou: Second Institute of Oceanography. 1-6.

[16] Li, H., Xu, F., Zhou, W., et al., 2017. Development of a global gridded Argo data set with Barnes successive corrections. Journal of Geophysical Research: Oceans. 122, 866-889.

[17] Shi, M.Ch., Gao, G.P., Bao, X.W., 2000. Method of ocean survey. Qingdao: Qingdao Ocean University Press. 51-52.

[18] Lu, S.L., Xu, J.P., Liu, Z.H., 2014. Analysis of the differences between microwave remote sensing SST and Argo NST in the Southern Hemisphere. Marine Forecasts. 31, 1-8.

[19] Liu, Z., Xu, J., Zhu, B., et al., 2006. Calibration of Argo profiling float salinity data using historical hydrographic data[A]. Hangzhou. Proceedings of "China Argo Science Workshop" Conference. 14-17.

[20] Chu, P.C., Fan, C.W., Liu, W.T., 2000. Determination of vertical thermal structure from sea surface temperature. Journal of Atmospheric and Oceanic Technology Meteorological Society. 17, 971-979.

[21] Chu, P.C., Fan, C.W., 2011. Maximum angle method for determining mixed layer depth from sea glider data. Journal of Oceanography. 67, 219-230.

[22] Zhang, C.L., Xu, J.P., Bao, X., 2015. Gradient dependent correlation scale method based on Argo. Journal of PLA University of Science and Technology (Natural Science Edition). 16, 476-483.

[23] Akima, H., 1970. A new method for interpolation and smooth curve fitting based on local procedures. Journal of the ACM. 17, 589-602.

[24] Juza, M., Penduff, T., Brankart, J.M., Barnier, B., 2012. Estimating the distortion of mixed layer property distributions induced by the Argo sampling. Journal of Operational Oceanography. 5, 45-58.

[25] Zhang, C.L., Xu, J.P., Bao, X., et al., 2013. An effective method for improving the accuracy of Argo objective analysis. Acta Oceanologica Sinica. 32, 66-77.

[26] Zhang, C.L., Wang, Z.F., Liu, Y., 2021. An argo-based experiment providing near-real-time subsurface oceanic environmental information for fishery data. Fisheries Oceanography. 30, 85-98.

[27] Lu, J., Qiao, F.L., Wei, Z.X., Teng, Y., Xia, C.Sh., 2008. Study on distribution of mixed layer depth in the world ocean in summer. Advances in Marine Science. 26, 145-155.

Sustainable Marine Structures
https://ojs.nassg.org/index.php/sms

REVIEW

Applications of Peridynamics in Marine Structures

Erkan Oterkus*

PeriDynamics Research Centre, Department of Naval Architecture, Ocean and Marine Engineering, University of Strathclyde, Glasgow, United Kingdom

ARTICLE INFO

Article history
Received: 30 December 2021
Accepted: 31 December 2021
Published Online: 10 January 2022

Marine environment is a harsh and challenging environment for both operators and analysers due to extreme weather conditions. As a result of these conditions, marine structures are subjected to extreme and/or cyclic loadings. This will then lead to various different damage modes including corrosion and fatigue. Such damage modes are major threats to the reliability and integrity of marine structures which can cause risk on human and environmental safety, and yield financial losses. Moreover, climate change is a major concern which requires urgent attention. In order to minimize the negative effects of climate change, energy transition from utilisation of fossil fuels to greener energy solutions, such as offshore wind, should be adapted. There is currently a rapid progress on investment on green technologies especially offshore wind energy generation. Another emerging area is hydrogen which is considered as the environmentally friendly fuel of the future.

There are various ways to produce hydrogen which are classified as grey, blue and green hydrogen production. Since CO_2 is also produced as part of the grey and blue hydrogen production, green hydrogen becomes the most environmentally friendly option. To produce green hydrogen, energy produced by offshore wind turbines can be utilised. A potential challenge of this approach is how to transport hydrogen to onshore. Utilisation of offshore pipelines can be an economical option. In addition, if there is already an existing infrastructure available for oil & gas applications, this can be even much preferable option without any need to install a new pipeline system. However, this requires extra care since these pipelines were not originally designed to transport hydrogen.

*Corresponding Author:
Erkan Oterkus,
PeriDynamics Research Centre, Department of Naval Architecture, Ocean and Marine Engineering, University of Strathclyde, Glasgow, United Kingdom;
Email: erkan.oterkus@strath.ac.uk

DOI: http://dx.doi.org/10.36956/sms.v4i1.475

Hydrogen can cause embrittlement problem, known as hydrogen embrittlement, especially for metallic structures and can cause cracking for loads much smaller than the design loads.

In order to minimize all the risks associated with the harsh marine environment and energy transition process, advanced computational methodologies should be utilised such as peridynamics as part of the analysis process. Peridynamics [1-4] is a new computational methodology which is especially suitable for failure analysis of materials and structures. Peridynamic equations are in the form of integro-differential equations and do not contain any spatial derivatives. Therefore, these equations are always valid regardless of discontinuities such as cracks. Definition of failure is pretty straightforward, and it is possible to analyse any number of cracks since cracks are not treated as special objects.

There are many application areas for peridynamics to be utilised in maritime field. One potential area is to use peridynamics for the analysis of ice-structure interactions [5-8]. There is currently an interest to use Northern Sea Route to ship products from Far East to Europe since this route is much shorter than the current route. However, ice-structure interaction is a major concern since ships should be designed by considering potential impact of ice pieces on ship hull which can cause significant damage to the ship hull as in the Titanic accident in the past.

Another important application of peridynamics is modelling the influence of underwater explosions on submarines or naval vessels. If an underwater explosion takes place, a shock wave is generated and this can cause significant damage to the structure. Predicting damage due to shock loading, especially if the structure is made from composite material, is challenging. Although composite materials have several advantages with respect to traditional metals, their failure behaviour is complex since different damage scenarios can occur including fibre breakage, matrix cracking, fibre-matrix splitting and delamination. Peridynamics is capable of accurately predicting these failure modes in structures subjected to different loading conditions including shock loading [9-11].

Another important application of peridynamics in marine structures is corrosion damage modelling. There are different corrosion mechanisms which can occur in structures due to material type, environment, and loading. One of the common corrosion damage mechanisms is pitting corrosion which creates localised damage in the structures. Pitting corrosion damage areas can act as stress raisers and cracks can initiate and propagate from these locations. From modelling point of view, this requires multiphysics and multiscale analyses to simulate coupled diffusion and mechanical fields by considering the microstructure which can be done in a single peridynamic framework [12,13]. Moreover, peridynamics can also simulate hydrogen embrittlement phenomenon as a stress corrosion cracking mechanism [14].

Fatigue is also an important damage mode in marine structures. S-N curve and Paris Law are common approaches which are utilised for fatigue analysis of marine structures. Fatigue damage is a complex process with three phases including fatigue initiation, fatigue crack propagation and final failure. S-N curve is capable to represent fatigue initiation and can provide fatigue life. However, it cannot predict how the fatigue damage evolves. Paris Law approach can predict how a fatigue crack can grow. However, it is not capable to predict fatigue initiation and final failure phases. As an alternative approach, peridynamics is capable of representing all three phases of fatigue damage [15-18] and can serve as a less conservative tool for the design and analysis of marine structures.

Finally, peridynamics can also be used for failure analysis of energy storage devices such as marine batteries [19] and fuel cells [20]. Such devices will serve an important role to reduce carbon emissions in future ships and make significant contributions to reach net zero targets. As a final note, peridynamics, as a new and emerging computational methodology, can be a suitable and alternative computational tool for failure analysis of problems relevant to marine structures applications.

References

[1] Silling, S.A., 2000. Reformulation of elasticity theory for discontinuities and long-range forces. Journal of the Mechanics and Physics of Solids. 48(1), 175-209.

[2] Silling, S.A., Askari, E., 2005. A meshfree method based on the peridynamic model of solid mechanics. Computers & structures. 83(17-18), 1526-1535.

[3] Silling, S.A., Epton, M., Weckner, O., Xu, J., Askari, E., 2007. Peridynamic states and constitutive modeling. Journal of Elasticity. 88(2), 151-184.

[4] Madenci, E., Oterkus, E., 2014. Peridynamic Theory and Its Applications. Springer, New York, NY.

[5] Vazic, B., Oterkus, E., Oterkus, S., 2020. In-plane and out-of plane failure of an ice sheet using peridynamics. Journal of Mechanics. 36(2), 265-271.

[6] Lu, W., Li, M., Vazic, B., Oterkus, S., Oterkus, E., Wang, Q., 2020. Peridynamic modelling of fracture in polycrystalline ice. Journal of Mechanics. 36(2), 223-234.

[7] Vazic, B., Oterkus, E., Oterkus, S., 2020. Peridynam-

ic model for a Mindlin plate resting on a Winkler elastic foundation. Journal of Peridynamics and Nonlocal Modeling. pp. 1-10.

[8] Liu, M., Wang, Q., Lu, W., 2017. Peridynamic simulation of brittle-ice crushed by a vertical structure. International Journal of Naval Architecture and Ocean Engineering. 9(2), 209-218.

[9] Diyaroglu, C., Oterkus, E., Madenci, E., Rabczuk, T., Siddiq, A., 2016. Peridynamic modeling of composite laminates under explosive loading. Composite Structures. 144, 14-23.

[10] Oterkus, E., Madenci, E., 2012. Peridynamic analysis of fiber-reinforced composite materials. Journal of Mechanics of Materials and Structures. 7(1), 45-84.

[11] Kilic, B., Agwai, A., Madenci, E., 2009. Peridynamic theory for progressive damage prediction in center-cracked composite laminates. Composite Structures. 90(2), 141-151.

[12] De Meo, D., Oterkus, E., 2017. Finite element implementation of a peridynamic pitting corrosion damage model. Ocean Engineering. 135, 76-83.

[13] De Meo, D., Russo, L., Oterkus, E., 2017. Modeling of the onset, propagation, and interaction of multiple cracks generated from corrosion pits by using peridynamics. Journal of Engineering Materials and Technology. 139(4), 041001.

[14] De Meo, D., Diyaroglu, C., Zhu, N., Oterkus, E., Siddiq, M.A., 2016. Modelling of stress-corrosion cracking by using peridynamics. International Journal of Hydrogen Energy. 41(15), 6593-6609.

[15] Silling, S.A., Askari, A., 2014. Peridynamic model for fatigue cracking. SAND2014-18590. Albuquerque: Sandia National Laboratories.

[16] Hong, K., Oterkus, S., Oterkus, E., 2021. Peridynamic analysis of fatigue crack growth in fillet welded joints. Ocean Engineering. 235, 109348.

[17] Nguyen, C.T., Oterkus, S., Oterkus, E., 2021. An energy-based peridynamic model for fatigue cracking. Engineering Fracture Mechanics. 241, 107373.

[18] Zhu, N., Kochan, C., Oterkus, E., Oterkus, S., 2021. Fatigue analysis of polycrystalline materials using Peridynamic Theory with a novel crack tip detection algorithm. Ocean Engineering. 222, 108572.

[19] Wang, H., Oterkus, E., Oterkus, S., 2018. Peridynamic modelling of fracture in marine lithium-ion batteries. Ocean Engineering. 151, 257-267.

[20] Wang, H., Oterkus, E., Celik, S., Toros, S., 2017. Thermomechanical analysis of porous solid oxide fuel cell by using peridynamics. AIMS Energy. 5(4), 585-600.

Sustainable Marine Structures
https://ojs.nassg.org/index.php/sms

ARTICLE

Thermal and Structural Behaviour of Offshore Structures with Passive Fire Protection

Sangchan Jo Erkan Oterkus*

University of Strathclyde, Glasgow, UK

ARTICLE INFO

Article history
Received: 30 December 2021
Accepted: 7 January 2022
Published Online: 30 January 2022

Keywords:
Passive fire protection
Thermal
Structural
Beam
Finite element method

ABSTRACT

In offshore structures, hydrocarbon fires cause the structure to loose its rigidity rapidly and this leads to structural integrity and stability problems. The Passive Fire Protection (PFP) system slows the transfer rate of fire heat and helps to prevent the collapse of structures and human losses. The vital design factors are decided in the detailed design stage. The determined design thickness must be accurately applied in the fabrication yard. However, there are many cases that the PFP is overused because of various reasons. This excessive application of the PFP is an unavoidable problem. Several studies have been conducted on the efficient application and optimal design of the PFP. However, the strength of the PFP has not been considered. In addition, research studies on the correlation between the thickness of the PFP and the structural behaviour are not widely available. Therefore, this study attempts to analyse the thermal and mechanical effects of the PFP on the structure when it is applied to the structural member. In particular, it is intended to determine the change in the behaviour of the structural member as the thickness of the PFP increases.

1. Introduction

The Passive Fire Protection (PFP) coating system is widely used in offshore topside structures to protect structures from hydrocarbon fires in both oil and gas industries. In particular, epoxy intumescent passive fire protection material has been used for the past 30 years. When a fire breaks out, the epoxy intumescent coating thickness increases and the coefficient of heat conduction of the coating decreases thereby slowing down heat transfer. The reduction in heat transfer prevents the protected structure from experiencing elevated temperatures from the fire. Epoxy passive fire protection materials are expensive and construction takes a lot of time and money. The weight is not negligible either. In order to solve these problems, various studies were conducted on the efficient application of passive fire protection and analytical techniques and procedures were developed for optimal design.

Amongst these, Kim et al. [1,2] performed nonlinear finite element analysis to analyse Floating Production Storage and Offloading (FPSO) topside structures subjected to

*Corresponding Author:
Erkan Oterkus,
University of Strathclyde, Glasgow, UK;
Email: erkan.oterkus@strath.ac.uk

DOI: http://dx.doi.org/10.36956/sms.v4i1.476

fire load. Friebe et al. [3] presented different case studies to demonstrate the effect of different applications of PFP on collapse time of an FPSO module structure. Sari et al. [4] used a risk-based method and compared against a conventional PFP optimisation method based on API RP 2FB and concluded that a risk-based approach can provide significant reduction of required PFP material. Lim et al. [5] presented a PFP material selection and optimisation process to reduce the impact of fire by considering different PFP material thicknesses. They indicated that cementituous material and cellular glass showed better fire prorection performance. Garaniya et al. [6] proposed a methodology to assess the effectiveness of passive fire protection by using Fire Dynamics Simulator. Paik et al. [7,8] performed full-scale fire testing to investigate the collapse of steel stiffened plate structures subjected to lateral patch loading with and without passive fire protection. In another study, Ryu et al. [9] presented new computational models to study fire-induced progressive collapse behaviour of steel stiffened plate structures with and without PFP. They developed transient thermal elastic-plastic large-deformation finite element models for this purpose.

The PFP coating system is designed based on fire risk analysis of the offshore structure. The effect of fire is assessed through sophisticated fire load assessments and CFD-based fire simulations. Based on these, the duration of each structural member's exposure to high temperatures can be calculated. Depending on its duration, the type and thickness of passive fire protection coating for each area are designed. Ambient conditions, materials, and structural composition of each structural member are also considered in the passive fire protection design.

However, there is one big issue in the application of passive fire protection; it is often applied more excessively than the design requirement. This is due to the geometric shape of the structural members, the surrounding fittings, and the skill of the workers. For example, about 20 to 30 mm of PFP is installed in the angle type beam to which 11 mm of PFP should be applied. It is one of the inevitable problems in the structural production process. This kind of thick passive fire protection causes unexpected interference with surrounding outfittings. In addition to that, the weight increase of the structure cannot be ignored due to its vast area of coverage. Significant additional cost of materials should also be considered.

Therefore, it is essential to determine the effect of the thick PFP itself on the structure. Moreover, it is important to investigate whether the PFP attached to steel has a positive effect on the thermal and mechanical behaviour of the steel structural members. To the best of authors' knowledge, the effect of PFP material properties on structural behaviour was not taken into account in earlier studies. Hence, this study aims to evaluate how the application of passive fire protection affects the thermal and mechanical behaviour of structural members. The effect of the change in the thickness of passive fire protection on the structure is examined. Possible positive effects besides the original function of the PFP applied to offshore structures are considered. For structural members with passive fire protection, finite element analysis is conducted for each condition before and during a fire.

2. Passive Fire Protection Systems

When a fire occurs and the temperature reaches 260-470 ºC, the Young's modulus of the steel is reduced by 40% [11]. In the case of a fire caused by flammable gas or liquid, it takes less than one second for the structure to reach this temperature. This can cause collapse of the structure.

The Passive Fire Protection (PFP) is one of the means used to prevent the premature destruction of steel structures in the event of a fire. The proper amount level of PFP is determined by the following factors: the size of the individual elements of the steel structure, the size of the member section, and the purpose of use.

This study considers the characteristics of epoxy PFP materials based on the Chartek 7 product, which is a widely used product in the offshore industry. The ingredients, which cause fire protection, are very similar across a broad spectrum of products [10].

2.1 Material Characteristics of Epoxy PFP

In the event of a fire, epoxy PFP material swells or intumesces. A layer of durable insulated char slows the rate of temperature rise on the steel substrates. The PFP materials protect the steel structure from reaching the critical core temperature within a certain period of time. The critical core temperature is the temperature at which the steel begins to loose its load capacity and it depends on the grade of the steel and the internal load requirements [12].

The PFP material is generally highly impervious to water ingress. It can also provide additional anti-corrosion features for the iron. Adhesion and strength are effectively improved by using flexible mesh together. It is tough, durable and resistant to impact and vibration damage. It does not require much maintenance [13].

Table 1 shows the material characteristics of Chartek 7 which is a representative product of passive fire protection materials. The density of 1.0 t/m^3 is much smaller than normal cement of 2.8 t/m^3 and similar to that of rubber of

0.93 t/m^3. The thermal conductivity of 0.213 W/m°C is superior to the concrete of 0.92 W/m°C and as small as the thermal conductivity of the wood of 0.2 W/m°C. The thermal properties such as the thermal conductivity and specific heat can be found in detail in Section 3.

Table 1. Material Characteristics of Epoxy PFP

Property	Value	Units
Density	1000	kg/m^3
Thermal Conductivity	0.213 (1.45)	W/m°C (Btu·in/hr ft^2°F)
Coefficient of Thermal Expansion	68×10^{-6} (38×10^{-6})	cm/cm°C (in/in°F)
Specific Heat	1.17 (0.28)	J/g°C (Btu/lb°F)
Moisture Absorption	3.3% non top-coated 1.4% top-coated	
Flame Spread	25.0	
Smoke Generation	130.9	
Toxicity Index	1.3	
Hardness	Typically 70	
Impact Strength / Inch of Notch	0.69 (0.10)	J/cm (ft·lb/inch)

2.2 Mechanical Properties of Epoxy PFP

Table 2 indicates the mechanical properties of Chartek 7. Its lap shear strength is 10 MPa and compressive strength is above 18 MPa. It is flexible and not affected by the deflection of the steel substrate for pre-erection applications. This material has a fully fire rated capability such as H-rated and J-rated for offshore platform applications [13].

Table 2. Mechanical Properties of Epoxy PFP

Property	Value	Units
Spray Applied Density	1000 (62.4)	kg/m^3(lb/ft^3)
Tensile Strength	12.8 (1850)	MPa (psi)
Tensile Modulus	1786 (259,000)	MPa (psi)
Compressive Strength	18.6 (2700)	MPa (psi)
Compressive Modulus	1172 (170,000)	MPa (psi)
Flexural Strength	22.8 (3300)	MPa (psi)
Flexural Modulus	1586 (230,000)	MPa (psi)
Lap Shear Strength	10.0 (1450)	MPa (psi)

3. Methodology

Primary and secondary members are subjected to passive fire protection because they can possibly be affected by fire loads in offshore topside structures. As mentioned earlier, PFP's main purpose is to help the structural member maintaining its function even at extreme temperatures of the rapidly rising hydrocarbon fire. The type and thickness of the passive fire protection system suitable for each component are finally determined in the process of the detailed design phase. Its thickness is usually determined from a minimum of about 3 mm to a maximum of about 18 mm. It is possible that it can be applied thicker in some different cases.

This study considers three types of PFP systems. Based on these, 44 case studies are considered to examine the thermal and mechanical characteristics of structural members with the PFP as the thickness of passive fire protection increases. The first analysis study explores the temperature distribution and thermal characteristics under different PFP coverage and thermal load conditions. This is done through transient analysis by applying the standard hydrocarbon fire curve. The second study is to perform linear static structural analysis for structural members with PFP in the absence of fire. In the third study, the behaviour of the PFP-applied structural members under both thermal and structural loads during the outbreak of fire is investigated. Finally, time-dependent thermal loads are applied to the columns subjected to compression in order to examine deformation and buckling characteristics.

3.1 Selection of Target Structures

Structures as shown in Figure 1 were considered to determine the application of passive fire protection and its impact on the behaviour of the structural members. The structural steel I-section beam is mainly used as a primary structural member to support various decks, gratings, pipes, and equipment in offshore platforms. Numerical analysis is carried out by dividing the state into no fire (i.e., no thermal load) and under fire conditions as:

A. The I-beam supports the steel deck as a primary structure. The underside of the steel deck is directly subjected to the heat of the fire. Therefore, the underside is covered with PFP. The top face of the I-beam is not covered with the PFP since it does not directly contact with fire heat.

B. The I-beam supports steel grating (or large equipment) as a primary structure. The I-beam does not have the PFP on the upper surface. In the event of a fire, the heat affects directly to all sides of the I-beam.

C. As a primary structure, the I-beam acts as a column. Thus, the compression force is applied to the top of the I-beam. Passive fire protection applies to all aspects. The thermal load from the fire is also applied to all sides of the I-beam.

3.2 Definition of Analysis Conditions

As given in Table 3, the analysis cases are set in groups of three and 44 different cases are considered. Transient

thermal and structural analyses were performed using ANSYS, a commercially available finite element analysis software [14]. The temperature distribution obtained as a result of heat transfer analysis was used as an input for the structural analysis.

Group A uses the plane element type to accurately identify the thermal distribution and characteristics of the I-beam section for hydrocarbon fire. Transient thermal analysis was performed with 200 time steps. Group B is a setting to identify the structural behaviour of the PFP-applied beam with the data obtained by thermal analysis. This coupled analysis was performed on the PFP-applied beams with six types of PFP thickness. Group C aims to examine the buckling behaviour of the columns subjected to compression. The vertical displacement caused by the compressive force can also be calculated. The buckling analysis considers "prestress effects" in the structural analysis process of a beam subjected to compressive force. Then, the characteristics of buckling can be evaluated by performing "Eigen Buckling" analysis.

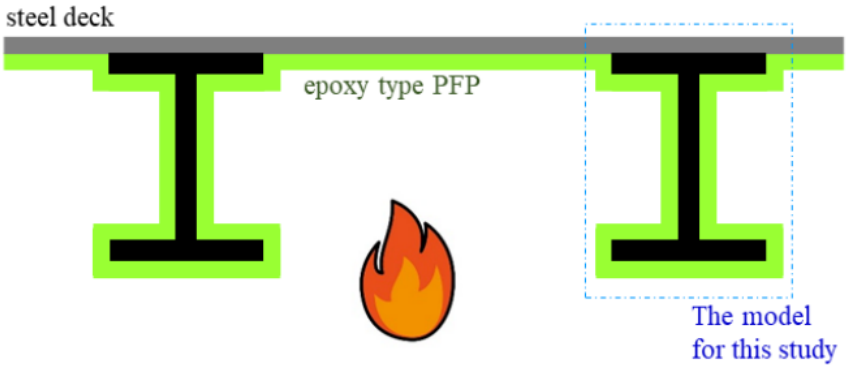

(a) I-beam Supporting the Steel Deck

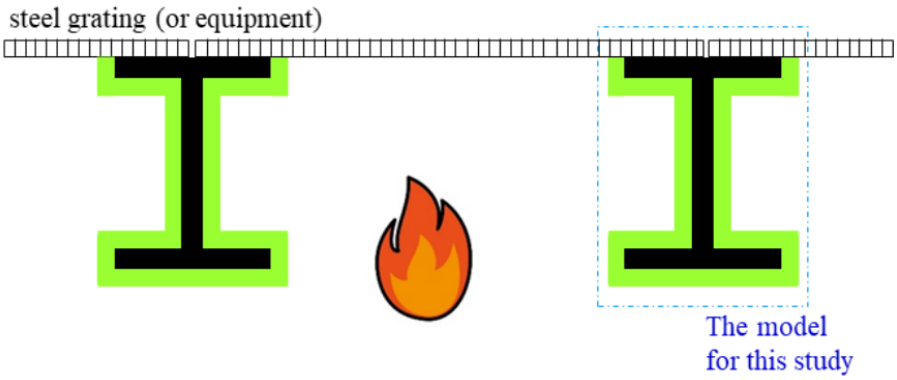

(b) I-beam Supporting the Grating (or Large Equipment)

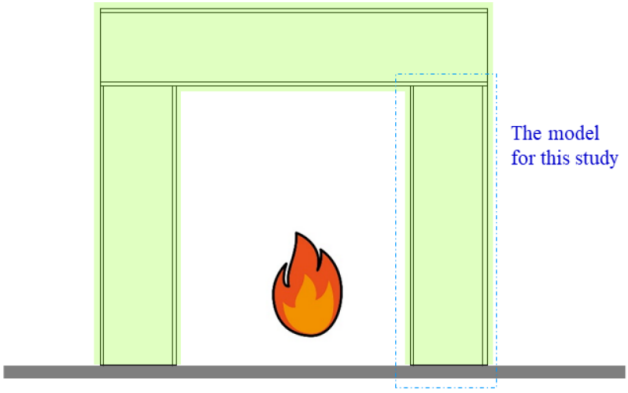

(c) I-beam as a Column

Figure 1. I-beam Frame with PFP

Table 3. Cases of the Numerical Analysis

Group	No.	PFP Thickness (mm)	Structural Load	Thermal Load	Numerical Analysis		Boundary Condition
					Type	Element	
A	TH3-00	0	Not applicable	Standard hydrocarbon fire	Transient/ thermal	Plane55	Not applicable
	TH3-01	1					
	TH3-03	3					
	TH3-06	6					
	TH3-10	10					
	TH3-15	15					
	TH4-00	0	Not applicable	Standard hydrocarbon fire	Transient/ thermal	Plane55	Not applicable
	TH4-01	1					
	TH4-03	3					
	TH4-06	6					
	TH4-10	10					
	TH4-15	15					
B	NFS-00	0	30 kPa	Not applicable	Static structure	Solid185	Fixed at both ends
	NFS-01	1					
	NFS-03	3					
	NFS-06	6					
	NFS-10	10					
	NFS-15	15					
	DF3-00	0	30 kPa	Standard hydrocarbon fire	Transient/ Structural thermal coupled	Solid70 Solid185	Fixed at both ends
	DF3-01	1					
	DF3-03	3					
	DF3-06	6					
	DF3-10	10					
	DF3-15	15					
	DF4-00	0	30 kPa	Standard hydrocarbon fire	Transient/ Structural thermal coupled	Solid70 Solid185	Fixed at both ends
	DF4-01	1					
	DF4-03	3					
	DF4-06	6					
	DF4-10	10					
	DF4-15	15					
C	NFB-00	0	Compression load 350 MPa	Not applicable	Static structure	Solid185	One end fixed Other free
	NFB-01	1					
	NFB-03	3					
	NFB-06	6					
	NFB-10	10					
	NFB-15	15					
	DFB-00	0	Compression load 350 MPa	Standard hydrocarbon fire	Transient/ Structural thermal coupled	Solid70 Solid185	One end fixed Other free
	DFB-01	1					
	DFB-02	2					
	DFB-03	3					
	DFB-04	4					
	DFB-06	6					
	DFB-10	10					
	DFB-15	15					

3.3 Application of Structural and Thermal Loading, and Boundary Conditions

Figure 2 shows the dimensions, structural loads, thermal loads, and boundary conditions based on the model demonstrated in Figure 1. In Figures 2 (a) and (b), 30 kPa of uniformly distributed load is applied to the upper surface of the I-beam over the entire length. The two ends of the member are assumed to be fully fixed. In case of Figure 2 (a), the fire heat on the top surface of the I-beam section is not taken into account in the numerical calculation. Figure 2 (b) is the setting in which fire heat is applied to all sides. The numerical analysis was performed by considering the symmetry condition. For Figure 2(c), a compressive load of 350 MPa was applied to one side of the cantilever beam. The other side is fully fixed.

The size of the member section used for all analyses is 200×100×10 (mm). The temperature by the standard hydrocarbon fire curve, indicated in Figure 3, was applied for 200 minutes under the conditions of each structural model [15].

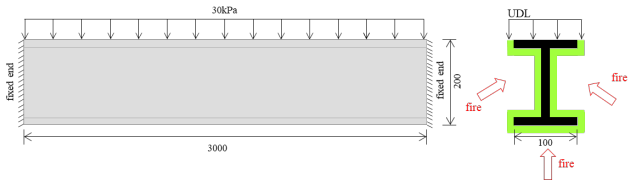

(a) I-beam with No fire on the Top Surface (DF3 analysis cases)

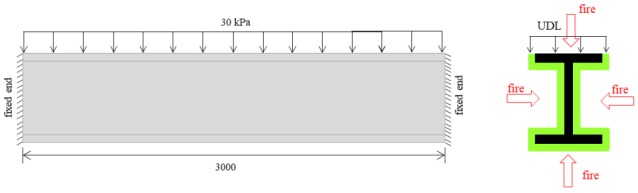

(b) I-beam with Fire on All Sides (DF4 analysis cases)

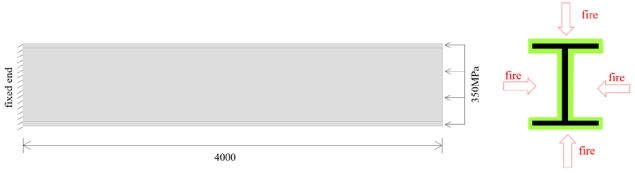

(c) I-beam as a Column with Fire on All sides (DFB analysis cases)

Figure 2. Configurations of the Steel Member for Analysis

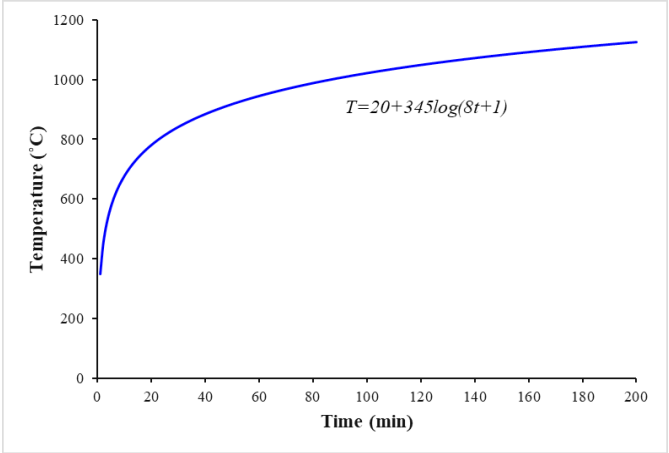

Figure 3. Standard Hydrocarbon Fire Curve

Figures 4 and 5 show the finite element models for the coupled analysis which are based on Figure 2. First, The SOLID70 elements were used for the transient thermal analysis and then SOLID185 was utilized for the structural calculation.

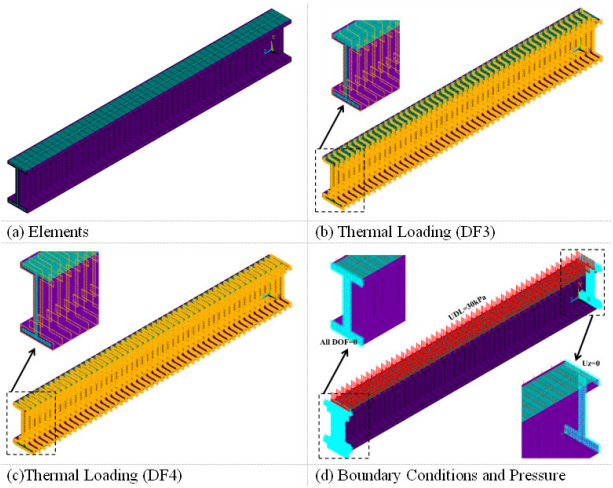

Figure 4. Finite Element models for DF3 and DF4 analysis cases

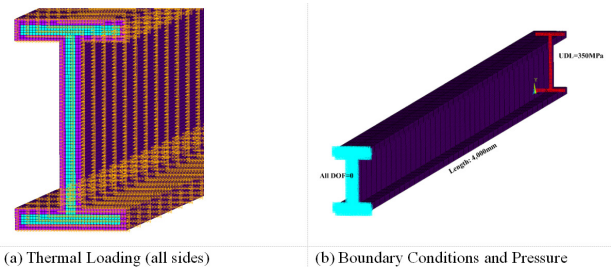

Figure 5. Finite Element model for DFB analysis cases

3.4 Material Properties

To examine the behaviour of the offshore structure

subjected to fire heat load, the dependency of materials on the temperature change must be defined [2]. In this study, specific heat, thermal conductivity, and elastic modulus values of each material were used for the numerical analysis.

3.4.1 Properties of Steel

The variation of specific heat (C_a, J/kg·K) of steel with temperature is given below and is represented in Figure 6 (a) as [11]

$$\text{for } 20^{\circ}\text{C} \le \theta_a \le 600^{\circ}\text{C}; C_a = 425 + 7.73\times10^{-1}\theta_a - 1.69\times10^{-3}\theta_a^2 + 2.22\times10^{-6}\theta_a^3 \quad (1a)$$

$$\text{for } 600^{\circ}\text{C} \le \theta_a \le 735^{\circ}\text{C}; C_a = 666 + \frac{13002}{738-\theta_a} \quad (1b)$$

$$\text{for } 735^{\circ}\text{C} \le \theta_a \le 900^{\circ}\text{C}; C_a = 545 + \frac{17820}{\theta_a - 731} \quad (1c)$$

$$\text{for } 900^{\circ}\text{C} \le \theta_a \le 1200^{\circ}\text{C}; C_a = 650 \quad (1d)$$

where, θ_a is the steel temperature [°C].

The variation of the thermal conductivity of steel (λ_a, W/m·K) with temperature is given below and is shown in Figure 6 (b) as [11]

$$\text{for } 20^{\circ}\text{C} \le \theta_a \le 800^{\circ}\text{C}; \lambda_a = 54 - 3.33\times10^{-2}\theta_a \quad (2a)$$

$$\text{for } 800^{\circ}\text{C} \le \theta_a \le 1200^{\circ}\text{C}; \lambda_a = 27.3 \quad (2b)$$

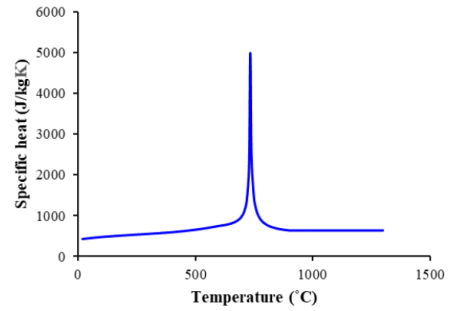

(a) Specific Heat

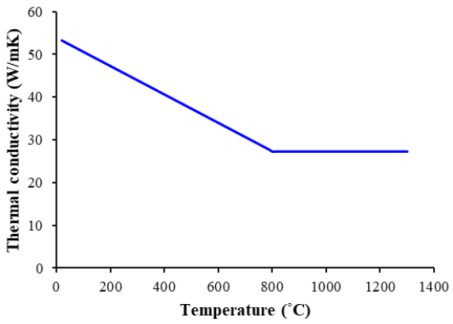

(b) Thermal Conductivity of Steel

Figure 6. Variation of steel properties with temperature

The change in Young's modulus of steel is shown in [11]. The modulus of elasticity of the steel does not change until the temperature reaches 100 °C, but it starts to decrease after that temperature. It is shown that it decreases by 40% at 500 °C and decreases by more than 90% at 800 °C.

3.4.2 Properties of the PFP Material

The specific heat of the epoxy type PFP material changes depending on the temperature as shown in Figure 7(a) [16]. This value decreases linearly as the temperature increases to around 1300 °C. Above 1300 °C, the rise of the temperature has no impact on the value. Figure 7(b) shows the change in thermal conductivity with increase in temperature of the PFP material. The thermal conductivity rapidly decreases at 150 °C. The change in both density and elastic modulus with the increase in temperature of the PFP material was not considered in numerical analysis due to the lack of information.

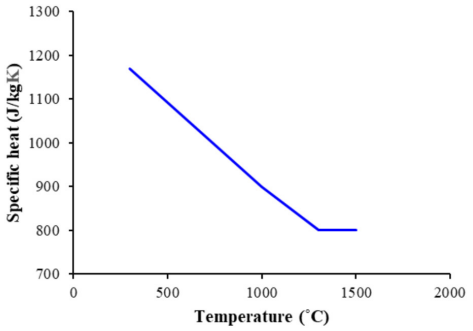

(a) Specific Heat

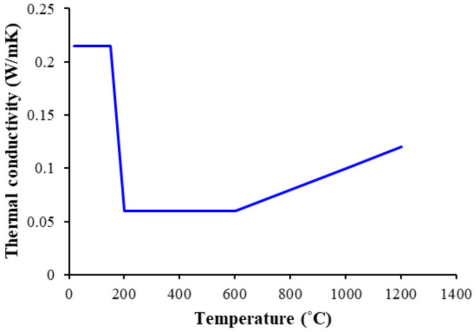

(b) Thermal Conductivity

Figure 7. Variation of properties of the epoxy type PFP material with temperature

4. Numerical Results

4.1 Analysis Group A

Generally, the conditions of fire protection for offshore structures are mainly applied for 60 minutes and 120

minutes. Therefore, Figure 8 shows the temperature distribution results of the I-beam section after 60 minutes of fire. Looking at the results of the TH3 cases, it can be seen that as the thickness of the PFP increases, temperature change in the beam section decreases significantly. In particular, when the PFP thickness is 15 mm, the heat of the fire hardly reaches the steel. Hence, it is determined that the PFP is completely slowing the heat transfer.

This trend can also be seen in the interpretation of TH4 cases on the top surface of the I-beam section without the PFP. The temperature rises rapidly. From the height of 100 mm to 200 mm of the section, it shows a constant temperature distribution due to the effect of the PFP.

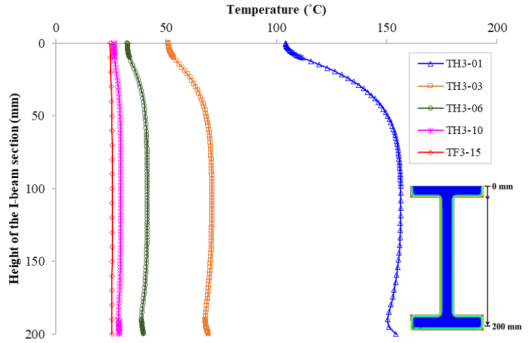

(a) TH3 analysis cases

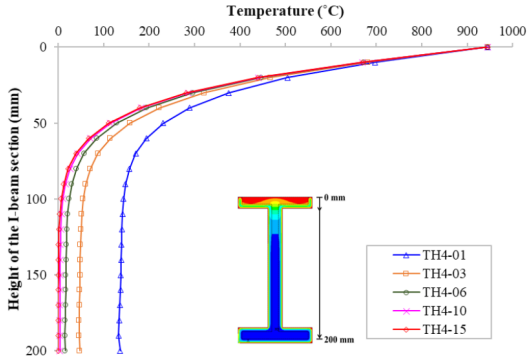

(b) TH4 analysis cases

Figure 8. Temperature distribution in the I-beam section after 60 minutes of fire

Figure 9 shows the temperature change over time at the midpoint of the I-beam. By comparing the two graphs when the PFP is not applied and when 1 mm thick PFP material is applied to the steel, it can be seen that the application of the PFP causes a significant delay in heat transfer even at very small thickness of PFP. Furthermore, it is confirmed that the rate of temperature change over time gradually decreases as the PFP becomes thicker.

In cases where the applied PFP is over 6 mm thick, the temperature increase over time is not much larger than the fire temperature. In particular, in the cases of TH3, the temperature does not exceed 100°C even at 200 minutes. The temperature tends to stay at an almost constant value. On the other hand, in TH4 cases, the rate of the temperature change with time is relatively large. Since 100 °C is the starting point of the change in the elastic modulus of the steel, this result is important.

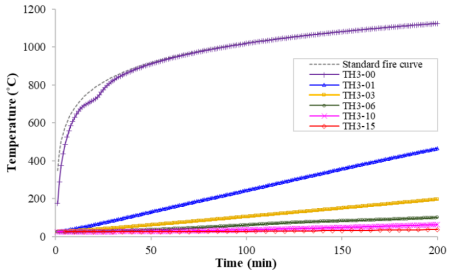

(a) TH3 analysis cases

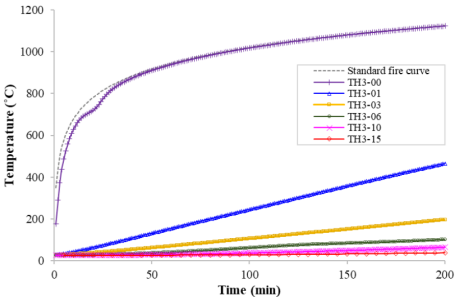

(b) TH4 analysis cases

Figure 9. Change in temperature over time (Center point of I-beam)

Based on the results above, the temperature of the steel was analysed 60 and 120 minutes after the fire occurred. As mentioned earlier, in the fire protection design for offshore structures, the conditions of 60 and 120 minutes defence time are the critical design criteria.

Figure 10 shows the temperature difference between the TH3 and TH4 analyses at the same PFP thickness after 60 and 120 minutes of fire. The average difference at 60 minutes is less than 10 °C. After 120 minutes, the difference is about 40 °C. If the structural member should be protected from the fire heat up to 60 minutes, the behaviour of the condition of the I-beam is not that dangerous even if the PFP is not applied on the top surface of it. It can also be seen that the thicker the layer of the PFP is, the smaller the difference is.

This result is very meaningful for the following reason. In terms of heat transfer under the design conditions of H60 or J60 fire rated, it can be seen that it is not important whether PFP is applied or not to the flange side of the I-beam section even when heat is applied to the steel from all directions.

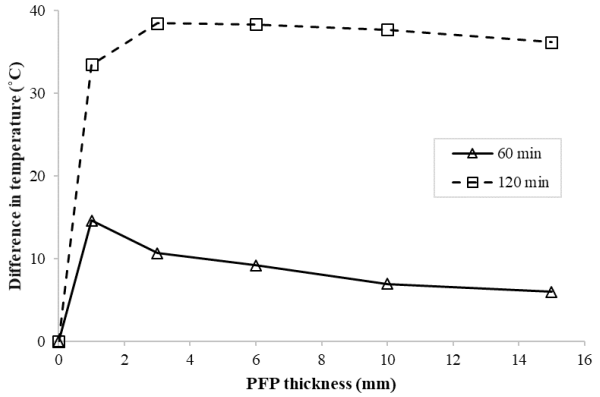

Figure 10. Temperature difference between TH3 case and TH4 case after 60/120 minutes of fire

Figure 11 shows the relationship between the temperature after 200 minutes of fire and the PFP thickness at the center point of the I-beam. It can be seen in Figure 11 that in both cases of TH3 and TH4, the temperature of the steel decreases as the PFP thickness increases. As the PFP thickness increases, the temperature change rate becomes smaller. Therefore, if the PFP is applied thicker than the appropriate thickness (which is judged to be 6 mm in this study), it is confirmed that increase of the PFP thickness does not significantly affect the reduction of the heat transfer.

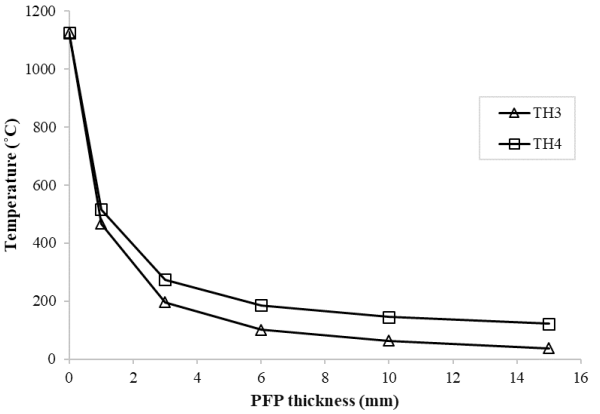

Figure11. Change in temperature with increase in PFP thickness (Center point of I-beam)

4.2 Analysis Group B

Regarding the behaviour of the PFP-applied beam during normal fire-free conditions, Figure 12 shows the change in vertical displacement at the center of the beam. When the PFP is applied, it appears that the deformation is increased by its weight. If self-weight is not taken into account, the application of a thicker PFP reduces the deformation of the beam. Therefore, the application of the PFP can increase the strength of the beam, but its weight causes the deflection of the beam.

Figure 13 shows the change in the vertical displacement value depending on the thickness of the PFP after 200 minutes of fire. In the range of 0 to 1 mm, the PFP layer plays a significant role regarding vertical displacement. There is a big difference between if the PFP layer exists or not. Even 1mm of the PFP material significantly lowers the heat conduction.

Although the displacement at the midpoint of the beam decreases in proportion to the increase in the PFP thickness, the reduction rate is not large. The main reason is that the PFP's own weight has a great influence on the beam behaviour. If the effect of self-weight of the PFP is limited, the increase in the thickness of the PFP layer can be interpreted in the sense that it reduces the deformation and increases the stiffness of the beam.

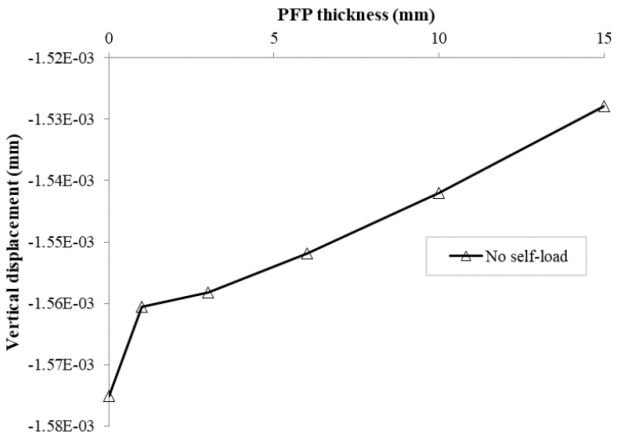

(a) Self-weight is not considered

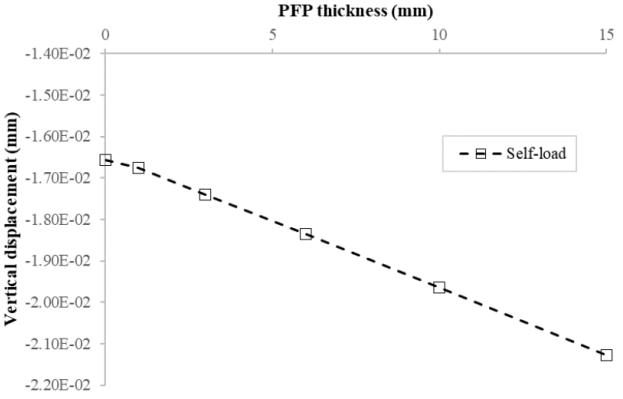

(b) Self-weight is considered

Figure 12. Beam deflection change in case of no fire

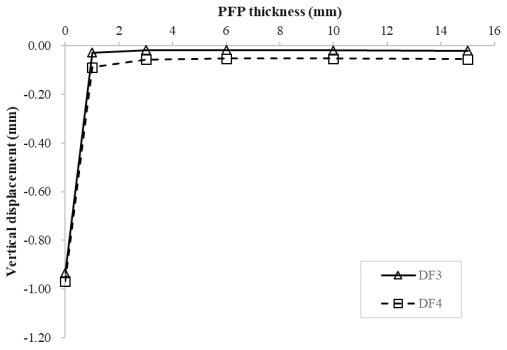

Figure 13. Comparison of the vertical displacement results after 200 Minutes of fire (Self-weight is considered)

Figure 14 shows the change in displacement over time. Here, it can be seen that the deflection of the beam is significantly reduced by applying the PFP. Also, the displacement tends to slightly increase as the PFP thickness increases. This is due to the self-weight of the PFP, as described above. In the case of DF3 analysis, the time-displacement is linear in most analysis cases because the PFP protects the beam from the thermal loads. In the analysis of DF4, the heat is transferred directly from the top of the I-beam where the PFP is not applied, so the deflection has a non-linear characteristic. In particular, looking at the DF4 analysis case, it can be seen that the rate of the time-displacement change increases at the point for about 100 minutes. The slope of the graph increases. After this point, the rate of the displacement change starts to increase and doubles at the end.

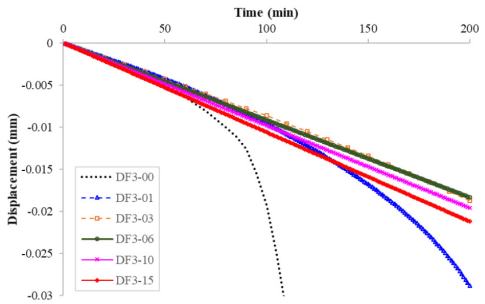

(a) DF3 Analysis Cases

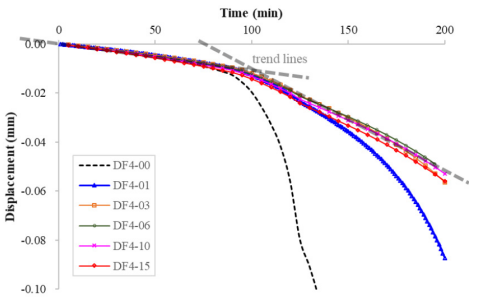

(b) Self-weight is considered

Figure 14. Time-displacement curve by PFP thickness during fire (Center of I-beam)

4.3 Analysis Group C

When the PFP was applied to a column subjected to axial compressive force, the deformation behaviour and buckling load of the column structural member were examined. This type of structure is commonly used in real offshore structures.

As shown in Figure 15, it is confirmed that the temperature of the steel does not exceed 100 °C since the PFP thickness is over 6 mm. Figure 16(a) shows the magnitude of displacement due to a compressive force according to the thickness of the PFP. In a fire-free situation (NFB), there is little change in deformation depending on the thickness of the PFP. However, the role of the PFP is obvious in the event of fire and heat. When the thickness of the PFP is less than 6 mm, the thickness of the PFP has a positive effect on the deformation of the beam. From the point where the PFP is 6 mm thick or more, the displacement is very similar to the case when there is no thermal load.

Similar trends can be seen in the BLF (Buckling Load Factor) values in Figure 16(b). The BLF is an index for evaluating the strength against the buckling of structures under compression. This coefficient is defined as the relative ratio of the critical load causing buckling divided by the compressive force exerted on the real object. In other words, a large buckling load factor indicates that the object is safe from buckling. The BLF value is significantly improved due to the application of the PFP. When a 6 mm thick PFP layer is applied to the beam, the buckling critical load increases by about 60 times compared to the case when there is no PFP layer.

For the PFP 6 mm thickness case, it shows a very similar value of the BLF value in case of no thermal load. In addition, as more PFPs are applied, it can be seen that the BLF value gradually increases. It can be seen that the PFP layer contributes to the increase in stability against buckling.

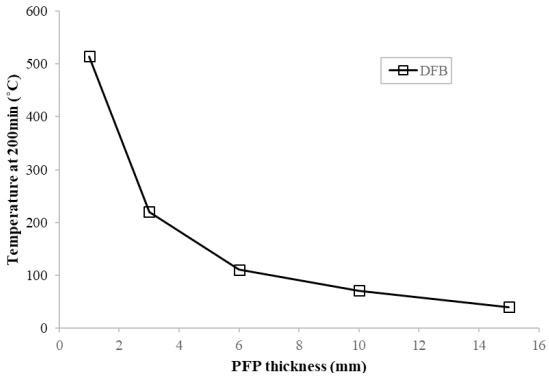

Figure 15. Temperature by PFP thickness in DFB Analysis (After 200 Minutes)

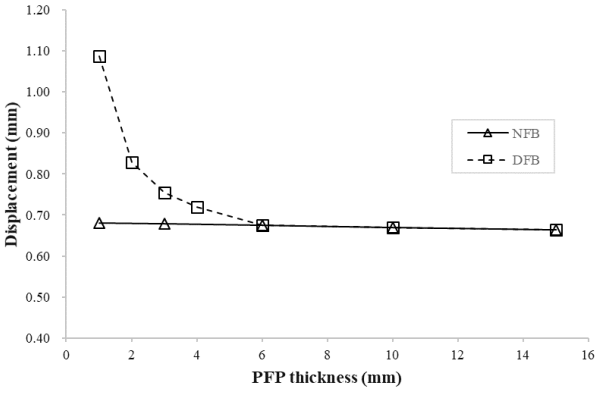

(a) Displacement

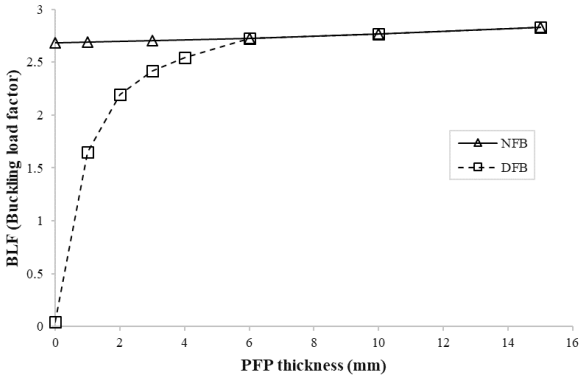

(b) BLF value

Figure 16. Displacement and BLF for each PFP thickness (Self-weight is considered)

Figure 17 shows the amount of compression displacement over time. The effect of applying the PFP to the four sides of the I-beam can be clearly seen by comparing DFB-00 and DFB-01. Even a very small amount of the PFP has a clear effect on reducing the heat transfer. In addition, as the PFP is applied thicker, the amount of heat transmitted to the steel is getting smaller. Therefore, there is no significant change in displacement.

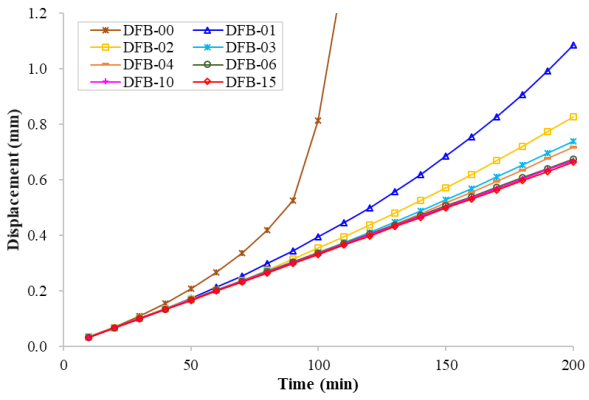

Figure 17. Displacement change by compression over time by changing PFP thickness

Here, it can also be seen that when the thickness is greater than a particular thickness, the effect of the increase in the amount of PFP on the deformation of the beam is reduced. The particular thickness value in this study can be determined as 6 mm and a larger amount of PFP than 6mm can be considered as overused. However, it is clear that even though the amount of reduction in deformation is small compared to the amount of the increased PFP, it contributes to the reduction in the deformation of the structural member.

5. Discussions

Various types of numerical analysis cases were considered for the PFP-applied beam. The research findings offer a new perspective on designing PFP for offshore structures.

According to the current study, the following points can be emphasized:

1) Large number of research studies have been conducted on the efficient use of the PFP and the optimized design of the PFP-applied structures. However, the strength of the PFP itself has not been considered. In this study, the structural behavior of the PFP-applied beam was analysed using the PFP tensile strength value. This is the beginning of a new perspective in the field of the PFP research.

The structural members which were analysed in this study is an I-beam. It is the most widely used primary member in offshore structures. Numerical analysis of 44 cases was considered by combining the PFP application condition, application thickness, and fire load application condition for this beam.

Coupled analysis was performed to simulate the actual structural member situation and includes thermal and structural analyses. Firstly, the thermal analysis was performed by inputting the time-dependent standard hydrocarbon fire temperature and the result was used for structural analysis. The temperature changes for 200 minutes and the structural behavior of the beam were analysed.

When performing the thermal analysis, the quality of the analysis result was improved by considering the temperature dependent properties such as specific heat and thermal conductivity. In structural analysis, the relationship between the safety of buckling and the application of the PFP layer was analysed by using the BLF value.

2) This study offers a new perspective. Efforts were made to find the positive effects of the PFP material which has no function on structures unless a fire breaks out. This attempt can contribute to the cost reduction of offshore

structures fabrication. The PFP is very widely applied to structures and it is often overused. If the technical data on the structural rigidity is inputted in the structural design, the effect of reducing the size of structural members can be expected. In addition, it would be possible to solve the problem of the excessive PFP application in the field. This study is the first step towards those goals.

3) This study considered the inclusion of the temperature-dependent material properties as much as possible. However, there is lack of information about temperature-dependency of some of the PFP properties such as the density and elastic modulus. For more accurate simulation of the PFP and beam behavior during a fire, studies on these two properties are definitely needed.

4) A mesh made by steel or fiber is one of the components of the PFP system. However, since the information on the mesh properties is not clear, the effect of it was not considered in this study. It will be necessary to study the mechanical properties of the mesh and include it in numerical analysis and experiments in the future.

6. Conclusions

PFP is widely used to help maintaining the integrity and stability of offshore structures for a certain period from hydrocarbon fires. In this study, the thermal and structural behaviour of PFP-applied beams before and during the fire was analysed using ANSYS.

The research findings can be summarised as:

1) From the results of heat transfer analysis, it was confirmed that in all cases, the application of PFP, even for a very small amount, significantly delayed the rate of heat transfer from the fire to the steel. The thicker the PFP, the greater reduction of the heat transfer takes place. However, when the thickness of PFP is greater than a certain value (6 mm), the effectiveness decreases.

2) A condition in which the PFP was not applied on the top surface of the I-beam was considered. Coupled analysis was performed on the cases where fire heat was directly transmitted to the top surface (DF4 analysis cases) and the case where it was not (DF3 analysis cases). As the thickness of the PFP increases, the deformation of the steel caused by heat decreases, but there is no significant change in the vertical displacement of the beam. Looking at the DF4 cases' results of the displacement of the I-beam over time, the rate of the displacement change increased by about 2 times after about 100 minutes.

3) The buckling analysis was performed on the PFP-applied column structure. It was confirmed that both the displacement and the BLF value caused by the compressive force were sufficiently improved until the PFP reached a certain thickness. In particular, when the PFP layer is applied to the I-beam, the critical buckling load is improved by about 60 times compared to the case without the PFP layer. However, after reaching a certain thickness, the amount of thermal load had little impact on both the displacement and the BLF value. This is related to the point when the temperature of the steel remains below 100 °C when the PFP is thicker than 6 mm.

4) This study will contribute to other further studies on the application of PFP as providing a new perspective to study structural analysis of PFP and beam composite.

Acknowledgement

This research is supported by PNU Korea-UK Global Program in Offshore Engineering(N0001288) funded by the Ministry of Trade, Industry and Energy.

References

[1] Kim, J.H., Kim, C.K., Islam, M.S., Park, S.I., Paik, J.K., 2013. A study on methods for fire load application with passive fire protection effects. Ocean engineering. 70, 177-187.
DOI: https://doi.org/10.1016/j.oceaneng.2013.05.017

[2] Kim, J.H., Lee, D.H., Ha, Y.C., Kim, B.J., Seo, J.K., Paik, J.K., 2014. Methods for Nonlinear Structural Response Analysis of Offshore Structures with Passive Fire Protection under Fires. Journal of Ocean Engineering and Technology. 28(4), 294-305.
DOI: https://doi.org/10.5574/KSOE.2014.28.4.294

[3] Friebe, M., Jang, B.S., Jim, Y., 2014. A parametric study on the use of passive fire protection in FPSO topside module. International Journal of Naval Architecture and Ocean Engineering. 6(4), 826-839.
DOI: https://doi.org/10.2478/IJNAOE-2013-0216

[4] Sari, A., Ramana, E., Dara, S., Azimov, U., March 2016. Passive Fire Protection PFP Optimization in Offshore Topsides Structure. In Offshore Technology Conference Asia. Offshore Technology Conference.

[5] Lim, J.W., Baalisampang, T., Garaniya, V., Abbassi, R., Khan, F., Ji, J., 2019. Numerical analysis of performances of passive fire protections in processing facilities. Journal of Loss Prevention in the Process Industries. 62, 103970.
DOI: https://doi.org/10.1016/j.jlp.2019.103970

[6] Garaniya, V., Lim, J.W., Baalisampang, T., Abbassi, R., 2020. Numerical Assessment of Passive Fire Protection in an Oil and Gas Storage Facility. In Advances in Industrial Safety. Springer, Singapore. pp. 1-21.

[7] Kee Paik, J., Ryu, M.G., He, K., Lee, D.H., Lee, S.Y., Park, D.K., Thomas, G., 2020. Full-scale fire testing

to collapse of steel stiffened plate structures under lateral patch loading (part 1)–without passive fire protection. Ships and Offshore Structures. pp.1-16. DOI: https://doi.org/10.1080/17445302.2020.1764705

[8] Paik, J.K., Ryu, M.G., He, K., Lee, D.H., Lee, S.Y., Park, D.K., Thomas, G., 2020. Full-scale fire testing to collapse of steel stiffened plate structures under lateral patch loading (part 2)–with passive fire protection. Ships and Offshore Structures. pp.1-12. DOI: https://doi.org/10.1080/17445302.2020.1764706

[9] Ryu, M.G., He, K., Lee, D.H., Park, S.I., Thomas, G., Paik, J.K., 2020. Finite element modeling for the progressive collapse analysis of steel stiffened-plate structures in fires. Thin-Walled Structures. pp.107262. DOI: https://doi.org/10.1016/j.tws.2020.107262

[10] Wade, R., March 2011. A Review of the Robustness of Epoxy Passive Fire Protection (PFP) to Offshore Environments. Corrosion 2011, Houston, USA. pp. 13-17.

[11] European Standard BS EN 1993-1-2:2005, 2010. Eurocode 3. Design of steel structures General rules - Part 1-2 Structural Fire Design.

[12] International Paint, 2014. Chartek Trusted epoxy passive fire protection. https://www.perge.cz/data/blob/product-application_pdf-20190630122600-8941-chartek-trusted-epoxy-passive-fire-protection.pdf

[13] International Paint, 2010. Chartek7 fireproofing. http://www.pfpsystems.com/assets/Uploads/C7Brochure0407001.pdf

[14] ANSYS, 2014. ANSYS Mechanical APDL Element References. ANSYS Inc.

[15] European Committee for Standardization (CEN), 2007. Eurocode 1: Actions on structures – Part 1-2: General actions – Actions on structures exposed to fire. EN 1991-1-2.

[16] Kim, M., Kim, G., Oh, M., June 2017. Optimized Fire Protection for Offshore Topside Structure with 3-Sides PFP Application. In The 27th International Ocean and Polar Engineering Conference, San Francisco, USA. pp. 25-30.

Sustainable Marine Structures
https://ojs.nassg.org/index.php/sms

ARTICLE

Effects of Antifouling Technology Application on Marine Ecological Environment

Liangcheng Liu[1] Ge Wang[2] Junyi Song[1] Bipu Hu[1*]

1. Department of Chemistry and Biology, College of Science, National University of Defense Technology, Changsha, 410073, China
2. Institute of Special Services, Naval Research Academy, Beijing, 102442, China

ARTICLE INFO

Article history
Received: 08 September 2021
Accepted: 10 January 2022
Published Online: 25 January 2022

Keywords:
Biological contamination
Antifouling technology
Marine ecological environment
The risk assessment

ABSTRACT

Resolving the contradiction between Marine economic development and Marine ecological environment protection has become an unavoidable and sharp problem. The uncontrolled use of Marine antifouling technology will bring uncontrollable and even irreversible damage to the Marine biosphere, which will lead to ecological disaster and threaten the survival of human beings. Therefore, it is an urgent task to find antifouling technology with lower environmental toxicity under the premise of considering economy. More attention should be paid to the long-term impact of mature and new technologies on the Marine ecological environment. This paper introduces the development status of antifouling technology, its influence on Marine ecological environment and puts forward the design strategy of comprehensive biological fouling prevention and control technology.

1. Introduction

With the increasing frequency of human marine activities and the construction of large-scale marine projects, marine fouling organisms will seriously threaten the safe and stable operation of marine facilities and cause greater economic losses. Humans have tried to explore marine antifouling technology by means of poisoning, coercion, avoidance, stripping and cleaning. At present, there is no antifouling technology that has the advantages of low cost, high efficiency, persistence, broad spectrum and environmental friendliness. Developing more green antifouling technology has become the world consensus.

The importance of marine environmental protection is self-evident, and the marine environmental pollution caused by economic development is increasingly prominent. The Maritime Environment Protection Committee (MEPC) of the International Maritime Organization (IMO)

*Corresponding Author:
Bipu Hu,
Department of Chemistry and Biology, College of Science, National University of Defense Technology, Changsha, 410073, China;
Email: 1508422574@qq.com

DOI: http://dx.doi.org/10.36956/sms.v4i1.438

has been committed to energy conservation and emission reduction of ships, improving the International Convention for the Prevention of Pollution from Ships and other conventions [1]. On March 3, 2011, China submitted its accession to the International Convention on The Control of Harmful Anti-Fouling Systems on Ships to the International Maritime Organization and took effect on June 7, 2011 [2]. In building a modern legal system for marine ecological and environmental protection, China has revised the Marine Environmental Protection Law four times, and issued more than 100 supporting regulations, departmental rules and local legislation. The widespread use of antifouling technology is one of the marine pollution sources that can not be ignored, and its impact on the marine ecological environment has attracted more and more attention of policy makers and scientific research institutions.

2. Application Status of Antifouling Technology

2.1 Harm of Fouling of Marine Organisms

Fouling of marine organisms mainly involves the formation of organic membranes by adsorption of organic molecules on the substrate, and the formation of biofilm by attachment reproduction of microorganisms [3]. Then, spores of algae, small fouling animals and larva of large benthic fouling organisms will attach and grow, and eventually form a large number of stable biological communities. In the development process of biological fouling from the early, middle and late stages, there is the phenomenon of attachment succession in the fouling community. In the end, micro and large fouling organisms usually form the fouling together, and it is often manifested as the aggregation and attachment phenomenon of some dominant fouling organisms, such as barnacles and mussels. However, in the actual environment, the formation process and apparent phenomena of defilement biomes are very complex and diverse, which are affected by various factors such as environment and competition between species, and are complicated with environmental conditions such as sea area, season, temperature and surface characteristics of materials [4].

The fouling of marine organisms mainly involves the formation of organic membranes by absorbing organic molecules on the substrate, and then the biofilm is formed by the attachment and reproduction of microorganisms. Then the spores of algae, small fouling animals and larva of large benthic fouling organisms will attach and grow, and eventually form a large number of stable biological communities. In the development process of biological fouling from the early, middle and late stages, there is the phenomenon of attachment succession in the fouling community. In the end, micro and large fouling organisms usually form the fouling together, and it is often manifested as the aggregation and attachment phenomenon of some dominant fouling organisms, such as barnacles and mussels. However, in the actual environment, the formation process and appearance of defilement community are very complex and diverse, which are affected by various factors such as environment and competition between species, and have complex relationship with environmental conditions such as sea area, season, temperature and surface characteristics of materials.

Barnacles, mussels, worms and other representatives of large Marine fouling organisms have both can secrete powerful underwater adhesion glue and the characteristics of calcium have hard shell, able to withstand high speed water erosion, the population is dominant in the community, the harm to Marine underwater installations, the largest is the main factors of ship sailing resistance increase [5]. Therefore, it has become the main research object in the field of marine pollution prevention. The most critical link for the occurrence of biological fouling is that larvae or algal spores are easy to attach themselves to underwater fixed facilities or anchored ships with relatively smooth water flow [6]. Biological fouling will increase the ship's sailing resistance, the most serious can increase the shaft power 84%, and accelerate the shell corrosion; The flow of seawater is reduced by blocking the seawater pipeline; Blocking aquaculture cage mesh and production reduction; Signal and transmission failures affecting underwater detection equipment. In freshwater basins, the main fouling organism is the Limnoperna fortunei [7], which is the most harmful to water transport projects, water conservancy projects and inland river navigation.

2.2 Principles of Marine Antifouling Technology

According to the scientific principle of antifouling technology, it is classified and introduced [8].

Physics-based antifouling technology has little impact on the environment, but it has great limitations in use and high energy consumption. Once physical conditions cannot be maintained, biological fouling will occur immediately. Mechanical removal refers to the removal of fouling organisms attached by underwater dynamic machinery instead of divers. Marine static facilities need continuous use. Cleaning before the ship docks can prevent biological invasion, and cleaning before leaving the port can timely prevent the development of early fouling and reduce treatment costs. Increasing flow rates and creating turbulence both work by creating a flow environment that adheres to the surface of the substrate and makes it difficult for the plankton larvae to attach; Increasing the surface temperature of the attached substrate will cause

the larva to escape, and the fouling organisms will die and fall off at the temperature that can not survive. The reduction of oxygen concentration is mainly aimed at the use of closed pipes. When oxygen concentration is lower than a certain value, the larva will lose its motor ability and cannot attach, and will cause the death of the attached contaminated organisms. Ultrasonic vibration makes it difficult for plankton larvae to attach and causes the shedding of early fouling organisms through the high-frequency vibration attached to the substrate [9]. Uv antifouling refers to the direct exposure of diode radiation or the embedding of the diode on the substrate of the high permeability UV coating. Uv radiation will cause DNA, RNA and protein denaturation, so that the fouling organisms lose their attachment ability or die [10].

Antifouling technology based on chemical principle has environmental toxicity, mainly divided into direct release antifouling agent and antifouling coating. The former is the early use of heavy metal ions or highly toxic pesticides as antifouling agents to kill a large range of contaminated organisms, and has been banned [11]. The latter has the advantages of high efficiency, broad spectrum, durability and low cost, and is the main antifouling technology means at present. Antifouling coating can be divided into biodegradable coating, fouling release coating (FRC) and self-polishing coating (SPC) according to the technical principle. Biodegradable coatings are mainly polyester polymer materials which can be degraded by biology and environment. The continuous degradation makes the contaminated organisms lose the binding site and desorption, but the service life is short because of continuous degradation. Fouling desorption coating is a kind of polymer material represented by silicone and fluoropolymer, which is difficult for fouling organisms to attach and easy to desorption due to its low surface energy and low modulus. However, its service life is limited by mechanical strength and underwater adhesion between substrate. The cations in seawater can be replaced by antifouling agent after hydrolyzing the polyacrylate silane ester resin base material in the self-polishing coating, so that the antifouling agent is released slowly, but the porosity will gradually increase. Humans have tried to screen antifouling agents by extracting antifouling active substances from marine animals, plants and microorganisms in large quantities, but high production cost, difficult grafting and easy degradation are the biggest limiting factors.

The antifouling technology based on biological principle mainly adopts biological suppression to limit the fouling of organisms by predation of natural enemies. This approach remains in the theoretical stage, because changing the stable abundance of organisms in the ecosystem or introducing alien species may cause secondary ecological disasters, and it is difficult to limit the activity range of the removal organisms, and the effect is slow. The removal organisms themselves are also affected by environmental changes. Bionical anti-fouling technology in recent years become a hot research topic, human through material micro-nano structure design and simulation of Lotus Leaf [12], Salvinia natans All, Sea anemones, Shark, fur animals, Andrias and so on antifouling mechanism [13], the structure has the characteristics of low surface energy, low modulus, in subsequent studies found creatures and antifouling secretion metabolic stop loss of anti-fouling ability of structure, Such technologies therefore need to address issues such as the high cost of manufacturing materials and the simulation of dynamic life processes.

3. Environmental Effects of Marine Antifouling

3.1 Current Situation of Marine Pollution

Due to its huge volume and strong self-purification capacity, the ocean is regarded as a "sea containing all kinds of pollution" by human beings. Ocean warming, acidification and accumulation of toxic substances are the most significant characteristics of its pollution [14], and the pollution of the upper coastal waters and tidal flats is the most serious. Direct economic losses mainly come from the reduction of aquaculture and fishing [15]. The exploitation and utilization of fossil fuels leads to the overload emission of greenhouse gases such as carbon dioxide, methane and nitrous oxide [16], which is the basic cause of global climate warming and ocean warming. Ocean warming will bring global ecological problems such as glacier melting and release of ancient viruses, land area shrinking due to sea level rise, irreversible degradation of coral reefs and other ecosystems [17]. Excessive fossil fuel use releases acidic gases such as Carbon dioxide, sulfur dioxide and Nitrogen oxides, which dissolve in water, causing ocean acidification and hindering the growth of calcareous skeletal shells of organisms such as crustaceans, coelenterates and mollusks. Toxic substances accumulate in water due to their stable chemical properties and most of them can be enriched in organisms, such as heavy metal ions, radioactive substances and microplastics, etc. Oil pollution will cause large-scale death of plankton and decrease of dissolved oxygen in water [18]. Therefore, marine pollution will bring about the compression of human living space and the destruction of food supply chain and other problems that threaten human existence.

Marine underwater facilities are one of the main sources of pollution. Nuclear power plants and nuclear-powered vessels will cause radioactive pollution [19]. Oil exploitation, transportation and ship navigation will produce

oil pollution. There are also industrial emissions of heat sources, ship navigation noise and other physical pollution and solid and liquid waste pollution.

3.2 Effects of Antifouling Coating Active Substances on Marine Environment

The polyester polymer materials in biodegradable coating are degraded into esters with low toxicity in water without forming residues [20]. It is worth mentioning that artificial synthesis of bacterial toxin butenolide extracted from Fusarium can block the fouling of biological attachment signal pathway rather than poison to achieve antifouling effect. The antifouling effect of the defiled-desorption coating depends on the physical properties of its material surface [21]. It does not release toxic substances. After the expiration of its life, the coating is scraped off for harmless treatment. The most harmful component to the marine ecological environment is the antifouling agent in the antifouling agent release coating [8]. Most antifouling agents are used in combination with cuprous oxide and organic biocides. Copper ions exist stably in free state in seawater and are difficult to be mineralized and precipitated. They accumulate in the environment and are enriched in the biological food chain. Long-term use will threaten the breeding of marine organisms and human food safety. Pyridinthione (PT) in the biocide will degrade to pyridine 1-ox-2-sulfonic acid with low toxicity in a short time [22], and the isothiazolinone derivative (DCOIT) can be rapidly oxidized and degraded to low toxicity in water, and finally converted to non-toxic substances without residue [23]. Irgarol 1051 (2-methyl sulfur-4-tert-butylamino-6-cyclopropyl amino-S-triazine) degrades slowly in water but is easy to photolysis [24]. It is most toxic to marine plants and has little effect on animals and bacteria. Antifouling agent release of antifouling paint in the base material and auxiliary materials of the pollution is small, the base material component polyacrylate silane ester resin, the main chain fracture hydrolyzed into low toxicity acrylate single molecule and is slowly degraded, will not remain as microplastics; Xylene in excipients is a class 3 carcinogen, which can degrade slowly in water and volatilize photodecomposition easily. It is not a persistent pollutant. N-butanol has a stronger paralyzing effect than ethanol, and it is not the main pollutant.

3.3 Impact of Other Antifouling Technologies on the Marine Environment

Physical antifouling has no residual harm, no environmental toxicity for fouling organisms, but the need for high energy consumption to maintain physical conditions may produce greater secondary pollution. High temperature antifouling requires a heat source to maintain the temperature of the base surface. Therefore, the continuous release of heat will increase the water temperature near the facility, causing the temperature stress effect on the surrounding aquatic organisms, and may affect the facility itself or the operator due to heat conduction. Because ultrasonic vibration can be widely spread in water, it may cause neurotic disorder of ultrasonic sensitive marine organisms such as dolphin, grouper, black bass and drum shrimp. Although there is no residual harm, the radiation area is wide, and it will also affect the precision instrument components and operators of facilities. Ultraviolet radiation causes nearby plankton die and biological exposed skin burns, a wide range of radiation attenuation in the water and won't cause pollution and no residue, but the extensive use of diode produces electronic garbage disposal costs and maintenance costs of circuit may be higher, so only apply to small underwater detection equipment.

In chemical antifouling, electrolysis of seawater produces hypochlorite ions and chlorine gas [25], which can directly kill plankton microorganisms, destroy the mucus on the body surface of fish and lead to electrolyte metabolism disorder in the body. Although non-toxic chloride ions can be rapidly converted, the electrochemical corrosion of the substrate will be accelerated, and energy consumption is also high. Analog enzymes, although they consume no energy, remain in the conceptual stage and are not discussed here. Bionic antifouling materials mostly do not release toxic substances, but the leakage of silicone oil from the porous structure will also cause oil pollution.

4. Management of the Use of Marine Antifouling Technology

4.1 Risk Assessment of Marine Antifouling Technology

Because the pollutants produced by immersion of antifouling coating have the characteristics of long half-life, accumulation and enrichment, strong toxicity and uncontrollable, the vast majority of laws and standards restricting the use of antifouling technology in the world are formulated for antifouling coating. The United States enacted the Toxic Substances Control Act (TSCA) in 1976; In 2006, THE European Union issued the Registration, Evaluation, Authorisation and Restriction of Chemicals (REACH), and in 2012, a new biocide regulation BPR-Biocidal Products Regulation replaced the original biocide directive BPD-Biocidal Products Directive. In 2017, China also issued national standards such as Risk Assessment Method for Marine Environment of Antifoul-

ing Active Substances used in Ship Antifouling Bottom Systems and Risk Assessment Method for Marine Environment of Ship Antifouling Bottom Systems Using Antifouling Active Substances.

The risk assessment procedure of antifouling coatings is firstly to screen substances [26], quantify the release rate and establish exposure scene model to obtain the predicted environmental concentration (PEC) to complete the exposure assessment. Then collect hazardous information for toxicity assessment and obtain environmental effect threshold (PNEC) to complete the risk assessment; Finally, all the information is integrated to carry out risk characterization to obtain risk entropy and form a risk assessment report. In recent years, the regulatory procedures for risk assessment and control of antifouling coatings have been basically and increasingly improved. The problem that needs to be solved is to perfect the model database of each sea area exposure scenario and construct various functional laboratory microcosmic models. In addition, the impact of other antifouling technologies on the marine ecological environment, especially precious and endangered species, should also be included in the evaluation scope.

4.2 Design Strategy of Marine Antifouling Technology

The biggest factor limiting new environmentally friendly antifouling technologies is cost control, and copper-containing antifouling paints are still dominant in the short term. It should be noted that the environmental toxicity of copper is much lower than TBT and other organotin antifouling agents, but the minimum effective permeability is more than 10 times of the latter. The cumulative effect of long-term use is uncontrollable and irreversible, which is obviously not a long-term solution. The AFS has banned organotin since 2008, and this year, the 76th Session of the International Maritime Organization's Marine Environmental Protection Committee (MEPC) adopted the AFS amendment. Use of Cybutryne (2-tert-butamino-4-cyclopropyl-6-methanethio-1,3, 5-triazine) in antifouling bottom systems will be prohibited from 1 January 2023. The leaching rate of copper ion is limited by the Technical Requirements for Environmental Marking Products - Antifouling Paints for Ships formulated by the Ministry of Environmental Protection of China. All over the world, the regulation of existing antifouling agents and the access of new antifouling agents will only become more stringent, and it is necessary to continue to look for antifouling agents with lower environmental and biological toxicity. Low cost bionic degradable antifouling agent and antifouling coating with dynamic surface matching use, forming multi-mechanism long-term static antifouling is an important direction of antifouling coating development.

The ultimate goal of antifouling is to achieve zero emissions only through physical structure and material surface properties. But in the real sense of the present environment-friendly antifouling technology has a variety of congenital defects, we can develop antifouling strategies through the macro level. To establish a database of the changing rules and characteristics of the fouling community in different seasons and sea areas, and to formulate a comprehensive anti-fouling strategy according to the dominant fouling organisms. On the premise of meeting the discharge standards, the pollutants discharged into the ocean are screened as antifouling agents, and local enrichment and discharge are carried out in antifouling parts to achieve antifouling effect, and the pollutants are reused. Comprehensive anti-pollution technology strategy should be considered in an overall way to find a balance between economic cost and risk management, so as to achieve lower overall toxicity and less consumption of pollutants produced by anti-pollution.

5. Conclusions

A large number of species extinction, seabed desertification, abnormal climate change, deterioration of coastal water quality, frequent fishing disasters have rung the alarm bell for human beings. Let us realize that it is urgent to solve the irreversible pollution problem, and we should comprehensively reduce the pollution caused by marine pollution prevention from multiple dimensions such as technological research and development, rational use, legal supervision and so on. Oceans connect all continents. Only by making joint efforts to protect and sustainably utilize oceans and marine resources can we maintain our common "blue granary" and "blue medicine storehouse". This is the only way for human civilization to continue to grow and flourish.

References

[1] Aldo, Ch., 2019. The IMO initial strategy for the reduction of GHGs from international shipping: A commentary(Article). International Journal of Marine and Coastal Law. 3, 482-512.

[2] Hassan, C.A.S.H., 2016. The Impact of Implementing the International Convention on the Control of Harmful Anti-fouling Systems in Ships (AFS Convention) on the Marine Environment. Shipbuilding and ocean engineering. 1, 57-63.

[3] Culver, C.S.A.B., Johnson, L.T.C., Page, H.M.B., et al., 2019. Integrated Pest Management for Fouling

Organisms on Boat Hulls. North American Journal of Fisheries Management.

[4] Dürr, S.P.W.D., Wahl, M., 2004. Isolated and combined impacts of blue mussels (Mytilus edulis) and barnacles (Balanus improvisus) on structure and diversity of a fouling community. Journal of Experimental Marine Biology and Ecology. 2, 181-195.

[5] Farkas, A., Degiuli, N., Martić, I., 2020. The impact of biofouling on the propeller performance. Ocean Engineering. 108376.

[6] Liang, Ch., Strickland, J., Ye, Z.H., et al., 2019. Biochemistry of Barnacle Adhesion: An Updated Review(Review). Frontiers in Marine Science.

[7] Wei, L., Xu, M.Zh., Zhang, J.H., et al., 2020. Survival and attachment of biofouling freshwater mussel (Limnoperna fortunei) to environmental conditions: potential implications in its invasion, infection and biofouling control. Limnology. 2, 245-255.

[8] Tian, L., Yin, Y., Bing, W., et al., 2021. Antifouling Technology Trends in Marine Environmental Protection. J Bionic Eng. 18(2), 239-263.

[9] Salta, M., Goodes, L.R., Maas, B.J., 2018. Bubbles versus biofilms: A novel method for the removal of marine biofilms attached on antifouling coatings using an ultrasonically activated water stream(Article). Surface Topography: Metrology and Properties. 3, 1-18.

[10] Ryan, E., Turkmen, S., Scopus Preview Benson, S.D., 2020. An Investigation into the application and practical use of (UV) ultraviolet light technology for marine antifouling(Article). Ocean Engineering. 107690.

[11] Amara, I., Miled, W., Slama, R.B., et al., 2018. Antifouling processes and toxicity effects of antifouling paints on marine environment. A review. Environmental Toxicology & Pharmacology. 115-130.

[12] Carve, M., Scardino, A., Shimeta, J., 2019. Effects of surface texture and interrelated properties on marine biofouling: a systematic review. Biofouling. 35(6), 597-617.

[13] Tian, L., Yin, Y., Bing, W., et al., 2021. Antifouling Technology Trends in Marine Environmental Protection. J Bionic Eng. 18(2), 239-263.

[14] Dobretsov, S., Coutinho, R., Rittschof, D., et al., 2019. The oceans are changing: impact of ocean warming and acidification on biofouling communities. Biofouling. 35(5), 585-595.

[15] Yigit, U., Ergun, S., Bulut, M., et al., 2017. Bio-economic efficiency of copper alloy mesh technology in offshore cage systems for sustainable aquaculture. Indian Journal of Geo-marine Sciences. 10, 2017-2024.

[16] Man, L., Feng, K.Sh., Zheng, H., et al., 2021. Supply chain effects of China's fast growing marine economy on greenhouse gas emissions. Environmental Research Letters. 5, 54061.

[17] Bradley, D.E., Andersson, A.J., Cyronak, T., 2014. Benthic coral reef calcium carbonate dissolution in an acidifying ocean. Nature Climate Change. 11, 969-976.

[18] Jin, Ch.H., Xu, Y.P., 2021. Risk Analysis and Emergency Response to Marine Oil Spill Environmental Pollution. IOP Conference Series: Earth and Environmental Science. 12070.

[19] M-Navarrete, J., Espinosa, G., I-Golzarri, J., et al., 2014. Marine sediments as a radioactive pollution repository in the world. Journal of Radioanalytical and Nuclear Chemistry. 299(1).

[20] Ma, Ch.F., Zhang, W.P., Zhang, Zhang, G.Zh., et al., 2017. Biodegradable Polymers; Studies in the Area of Biodegradable Polymers Reported from Hong Kong University of Science and Technology (Environmentally Friendly Antifouling Coatings Based on Biodegradable Polymer and Natural Antifoulant). Journal of Engineering.

[21] Hu, P., Xie, Q.Y., Ma, Ch.F., et al., 2020. Silicone-Based Fouling-Release Coatings for Marine Antifouling. Langmuir : the ACS journal of surfaces and colloids. 36(9).

[22] Zhi, Y.S., Jung, J.H., Jang, M., et al., 2019. Zinc Pyrithione (ZnPT) as an Antifouling Biocide in the Marine Environment—a Literature Review of Its Toxicity, Environmental Fates, and Analytical Methods. Water, Air, & Soil Pollution: An International Journal of Environmental Pollution. 230(4).

[23] Heloísa, B.G.A., Da-Silveira-Guerreiro, Juliana, Z.S., 2021. Molecular and biochemical effects of the antifouling DCOIT in the mussel Perna perna. Comparative Biochemistry and Physiology, Part C. 239.

[24] Zhang, A.Q., Zhou, G.J., Lam, M.H.W., et al., 2019. Toxicities of the degraded mixture of Irgarol 1051 to marine organisms. Chemosphere. 565-573.

[25] Gaw, Sh.L., Sarkar, S., Nir, S., et al., 2017 Electrochemical Approach for Effective Antifouling and Antimicrobial Surfaces(Article). ACS Applied Materials and Interfaces. 31, 26503-26509.

[26] Karina-Lotz-Soares-A, C., Sergiane-Caldas-Barbosa, C., Ednei-Gilberto-Primel, C., et al., 2021. Analytical methods for antifouling booster biocides determination in environmental matrices: A review. Trends in Environmental Analytical Chemistry. e108.

NASS
NAN YANG ACADEMY OF SCIENCES

Sustainable Marine Structures
https://ojs.nassg.org/index.php/sms

SHORT COMMUNICATION

Functionally Graded Material and Its Application to Marine Structures

Chandrasekaran, S.[1*] Hari, S.[2]

1. Department of Ocean Engineering., IIT Madras, Chennai, India
2. School of Petroleum Technology, Pandit Deendayal Petroleum University, Gandhinagar, India

ARTICLE INFO

Article history
Received: 14 February 2022
Accepted: 21 February 2022
Published Online: 28 February 2022

Keywords:
Marine structures
Functionally graded materials
Marine riser
Offshore structures
Form-dominant design

ABSTRACT

Marine structures are exposed to harsh weather conditions, demanding special pre-requisites in design and functional perspectives. Under dynamic loads of larger magnitude, the material-centric design procedure alone is not feasible to ensure the safe disbursement of loads. The compliant offshore structures resist loads primarily by their geometric novelty, and hence their design is form-dominant and no more strength (material) dominant. Large displacements in the rigid body modes in the horizontal plane under lateral loads require their construction material to possess enough ductility to absorb this energy. Steel is one of the most competitive materials for marine structures as it offers good ductility, but corrosion in the marine environment is a major concern. It undergoes strength and functional degradations and therefore requires serious investigation. In the present study, functionally graded material (FGM) is proposed to substitute for steel in marine applications. The method of fabricating FGM and assessing its mechanical and durability properties are discussed. Results show that FGM possesses strength and durability properties at par with the conventionally used X52 steel for marine risers. The presented study will be a major initiative towards future research in exploring competent materials which will be strong and sustainable in the marine environment.

1. Form-dominant Design Approach

Offshore structures are intended to perform oil and gas exploration under the marine environment while facing many challenges in extreme load combinations, sustainability against the corrosive environment, and a quick return on investment (RoI) [1,2]. The exploration activities towards ultradeep water and arctic regions induced a paradigm shift in their design procedures [3]. Advances in technology and industry maturity make deep-water oil and gas exploration an attractive investment. Furthermore, wind and wave energy have become the recent focus and pivotal points of attraction for green energy harvest. Environmental loads that arise from

*Corresponding Author:
Chandrasekaran, S.,
Department of Ocean Engineering., IIT Madras, Chennai, India;
Email: drsekaran@iitma.c.in

DOI: http://dx.doi.org/10.36956/sms.v4i1.490

waves, wind, and current become more severe in ultra-deepwater. Offshore engineers are increasingly deploying compliant systems that are permitted to undergo large displacements. For example, exploratory and production drilling has become more comprehensive with the recent developments in the design of semi-submersibles [4]. Effective design methods, based on the postulated failure analyses help arrive at the safer and sustainable design of platforms for extreme ocean conditions. The natural periods and damping ratios for the Semi-submersible at 1500 m and 2000 m water depths, with and without a submerged buoy, are obtained from free-oscillation tests; results are shown in Table [5]. It is seen that considerable periods in the surge, sway indicate higher flexibility about the horizontal plane. In contrast, small periods in roll, pitch, and heave show that they are stiff in the vertical plane. By this compliant approach in the design, natural periods in sway and yaw are found to be increased, along with a significant increase in the damping ratios for the surge, pitch, and yaw in the presence of a submerged buoy. It is interesting to note that a semi-submersible platform is usually characterized by possessing free modes, indicating that the natural periods in all degrees of freedom are above the wave periods [6]. Postulated failure analysis for compliant platforms helps investigate the failure modes under extreme conditions to assess their survivability. Surge response is significantly higher in the case of postulated failure of mooring lines. Addition of buoy at an appropriate location in the mooring help to reduce the response of mooring lines [4]. Surge response, which is the controlling factor for design is significant in the absence of submerged buoys.

Compliant offshore platforms are designed to resist lateral loads from waves, current and wind by their innovative geometric form. See, for example, Tension Leg Platform (TLP), Spar, Triceratops, and semi-submersibles. Out of the six degrees of freedom exercised by the rigid body motion of these platforms, two translational and one rotational degree, namely surge, sway, and yaw, are very flexible, exhibiting considerable periods. It makes the platform flexible in the horizontal plane and enables it to resist the lateral loads by undergoing large displacements. The remaining degrees of freedom, namely heave (translational in Z-axis) and roll and pitch (rotational), exhibit very stiff behaviour and make the platform rigid in the vertical plane. Such hybrid motion characteristics are salient features of compliant platforms. Let us consider a TLP, whose conceptual figure is shown in Figure 1; a figure of Neptune TLP shown by the side gives an idea of various structural components. It consists of vertical columns and pontoons designed as tubular members to enhance buoyancy. As the design concept conforms to the fact that buoyancy shall exceed the weight of the platform, it is position-restrained by tethers, which are under axial pretension to balance the excessive buoyant force. As a result, motion on the vertical plane such as heave, pitch and roll are restrained while it allows large displacements along with surge, sway and yaw degrees-of-freedom.

Table 1. Dynamic characteristics of moored Semisubmersible [5]

Description			Surge	Sway	Heave	Roll	Pitch	Yaw
Without buoy	1500 m water depth	Tn (s)	209	165	21	24	25	49
		ζ (%)	6.15	6.92	2.47	2.97	0.93	6.51
	2000 m water depth	Tn (s)	193	184	25	25	25	54
		ζ (%)	5.84	6.38	4.15	4.75	1.91	7.98
With buoy	1500 m water depth	Tn (s)	195	183	21	23	24	54
		ζ (%)	6.56	6.77	1.20	1.44	1.32	10.36
	2000 m water depth	Tn (s)	213	199	21	23	24	53
		ζ (%)	6.87	6.21	1.45	1.06	0.83	4.61

As seen in Figure 2 [7], which illustrates the TLP mechanics, a strong coupling is seen between surge (offset) and heave (set down) motion. Large displacements along surge invoke a supportive resistance from heave motion, which helps to encounter the lateral loads. This form-dominance characteristic makes their design unique, imparting a design shift from material strength-dominant to form-dominant. In addition, the horizontal components of the increased tension in the tethers help the platform return to its equilibrium position under the presence of loads. It is referred to as recentering, and geometric stability is imposed by the recentering ability taught in the design. Another classic example is the triceratops, shown in Figure 3 [7]. Offshore triceratops is a new generation of offshore platforms that are intended for use in ultra-deep waters. The deck of the platform is supported by the buoyant legs, which are, in turn, anchored to the seabed using pre-tensioned tethers. Ball joints are placed between the deck and the buoyant legs (please, see Figure 3), which partially isolate the deck from the buoyant legs and help counteract the lateral loads and moments [8]. These ball joints transfer only the translations from the legs to the deck and vice-versa; they restrain the moment's transfer and thus partially isolate the deck from the buoyant legs. Such design methods are often referred to as FORM-dominant design, which forms the basis for most of the compliant offshore structures.

Large displacements of such compliant structures demand a ductile material to absorb these motions without

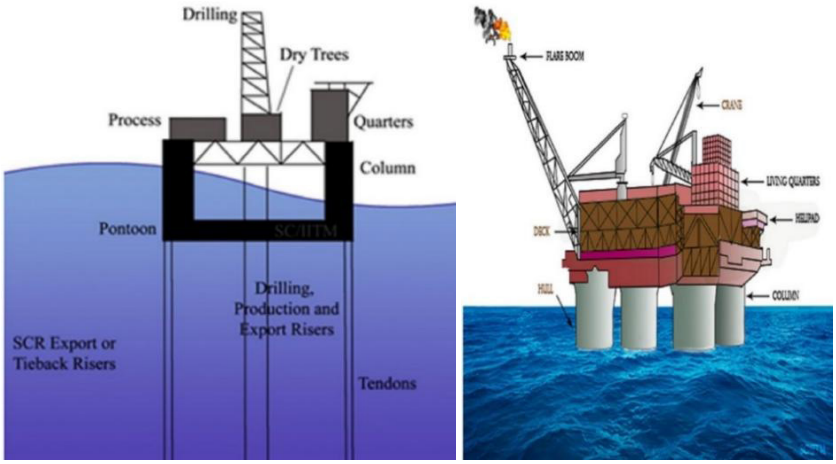

a) conceptual figure b) Neptune TLP [3]

Figure 1. Offshore Tension Leg Platform

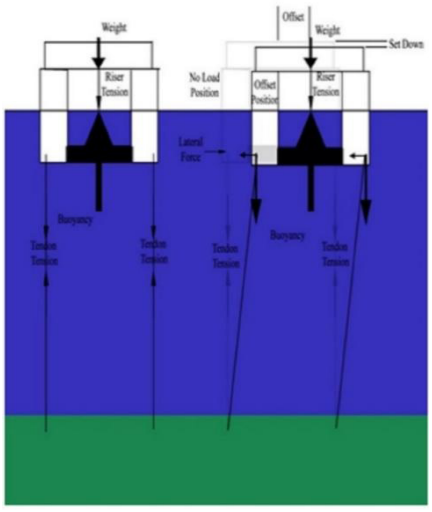

Figure 2. TLP mechanics

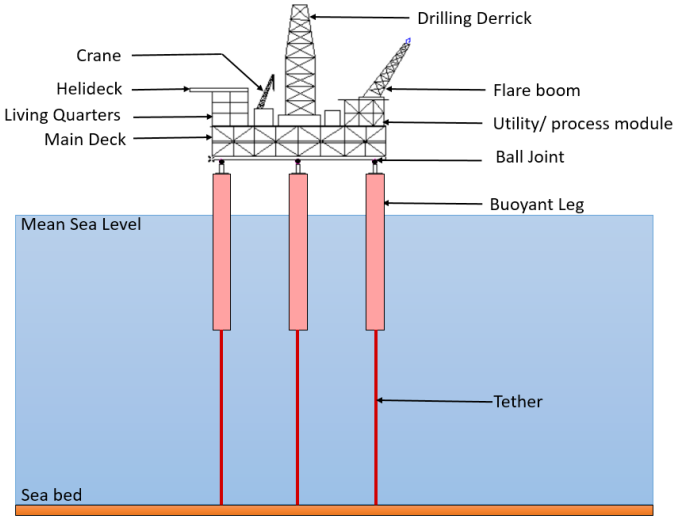

Figure 3. Offshore Triceratops

any strength degradation [1,2]. Although steel is recognised as the most suitable material, it corrodes in the marine environment. Hence, in addition to the desired strength requirements, materials for marine structures should also possess desirable functional requirements for their sustainability in the marine environment. A few of them are namely corrosion-resistance, anti-biofouling, and non-toxic. No single material can meet all such challenges of functionally and structurally excellent. Furthermore, even if such materials are manufactured, they cannot be used to construct marine structures unless the design codes of practices recommend them. Therefore, the current trend is to address the design by strength considerations and fulfil others using chemical or biological treatments. As a result, the sustainability of marine structures encounters a bi-fold problem: one concerning strength degradation and the other is the functional degradation under ageing. This challenge faced by the marine structures during their service life needs to be addressed to make them sustainable and functional.

2. Functionally Graded Material

Functionally graded materials (FGM) are useful in the Defence, aerospace, and medical field; recent attempts are made to assess their use in the marine environment [9]. Process industries where pipelines are subjected to corrosion under chlorides and sulphides, many mechanical components and appurtenances are replaced with FGM [10]. FGM is a novel material manufactured by functionally-grading two metal components, which are chosen based on strength and corrosion resistance. Manufacturing

such materials is a big challenge as the manufacturing process shall impose significant challenges in achieving the desired properties of FGM [11]. In the manufacturing process of FGM, materials of desired characteristics are chosen, and their geometric compositions (not the metallurgical composition), in terms of thickness and number of layers, are varied continuously across the cross-section. Thus, the composition and microstructure are altered along the cross-section to generate the desired property gradient. It is intended to utilise completely the mechanical, metallurgical and structural properties of the original materials while forming the FGM [12]. The wire arc additive manufacturing method (WAAM) enables the metallurgical composition of user-defined materials by a step-wise addition [13]. The component metals are deposited in layers in wires, while an electric arc is used as the heat source. Metallic wires are advanced using a secondary wire-feeder at the desired speed. A high-pulse current is supplied to form an arc between the electrode wires and the substrate, resulting in the melting of the filler tip of these advancing wires. A stainless-steel substrate is used to deposit the materials, while a high-power source is used for the deposition process. Figure 4 shows various components of the WAAM unit, namely the Cold Metal Transfer (CMT) torch, the substrate and the CNC machine integrated with the torch. The deposition parameters for the WAAM process are based on the constituent materials and the appropriate fillers.

Marine risers are subjected to severe corrosion in the presence of hydrogen sulphide and chlorides. Further, stress corrosion is accelerated due to the high-pressure and high-temperature conditions [14]. Hence, marine risers are a classic example of structural members under stress concentration and corrosion. X-52 steel is a common candidate for marine risers. In the present study, X-52 carbon-manganese steel is graded with duplex stainless steel to manufacture FGM on the lab scale. The chosen materials are code compliant for marine structures [15,16]. While duplex stainless steel possesses a higher corrosion resistance in acidic conditions, X-52 steel is a good strength contributor. As discussed in the earlier section, materials for FGM are chosen based on the functional requirements, namely strength and corrosion resistance.

Figure 5 shows the cross-section of the riser under investigation, where the inner layer of 3 mm is duplex stainless steel, and the rest of 14 mm is carbon manganese steel. The sizing of the riser is as per the existing riser of Auger TLP [17]. X-ray computed Tomography test on the FGM build confirmed that it is free from porosity and micro-cracks. FGM build, extracted from the manufactured specimen, is shown in Figure 6, where the optical markers are made to assess the longitudinal and lateral strain during the tension test. It is important to note that loading is applied parallel to the interface of the materials to observe its behaviour at the critical interface (Please see, Figure 7).

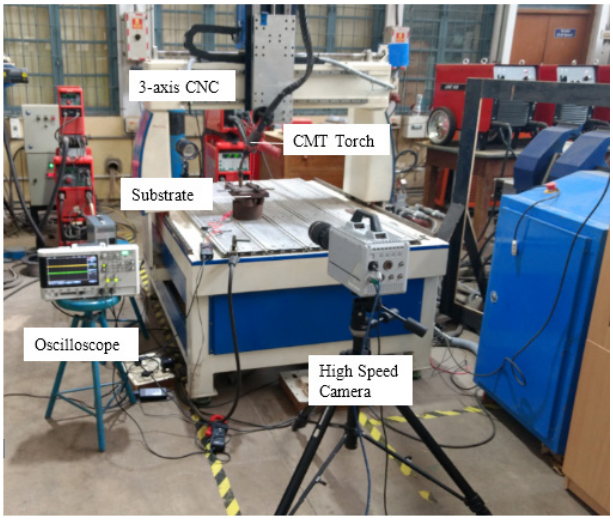

Figure 4. WAAM unit used to manufacture FGM.

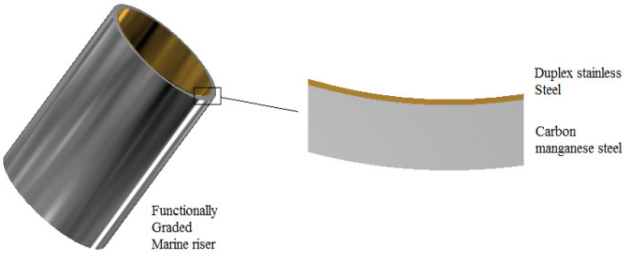

Figure 5. Cross-section of riser under investigation

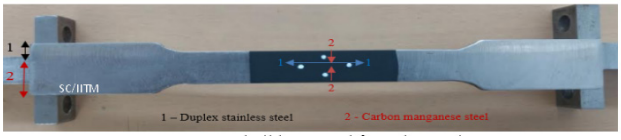

Figure 6. FGM build extracted from the specimen.

The tension tests are carried out on the FGM specimens at a strain rate of $1x10^{-3}$ s^{-1}. The ultimate strength of FGM samples is about 600 MPa, while the yield strength is about 400 MPa, with the modulus of elasticity computed as 213 GPa. Compared with X-52 steel, one can observe a significant increase in the ultimate and yield strength with a very high ductility ratio. Results are summarised in Table 2. As seen in Figure 9, the fractured sample confirms that the failure is not along with the interface of the constituent metals but similar to structural grade steel.

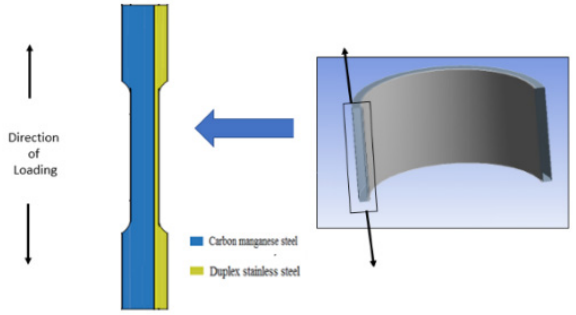

a) load direction

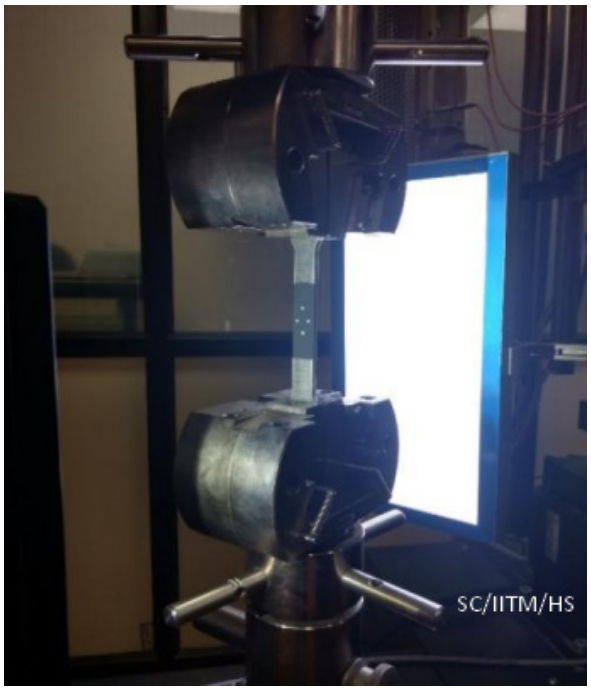

b) loaded specimen

c) fractured specimen

Figure 7. Tension test

At the interface of the constituent metals, an elemental line energy dispersive X-ray analysis (EDX) is carried out to determine the chromium variation along with the interface. Figure 9 shows the EDX image, which verifies that the chromium content in duplex stainless steel is about 22% at 35 microns from the interface, and it is closer to the duplex stainless steel side. It offers corrosion resistance to FGM. X-ray diffraction analysis (XRD) resulted in an output confirming a prominent peak of (Cr 0.1, Fe 1.9) indicating the presence of chromium oxide at the interface regions.

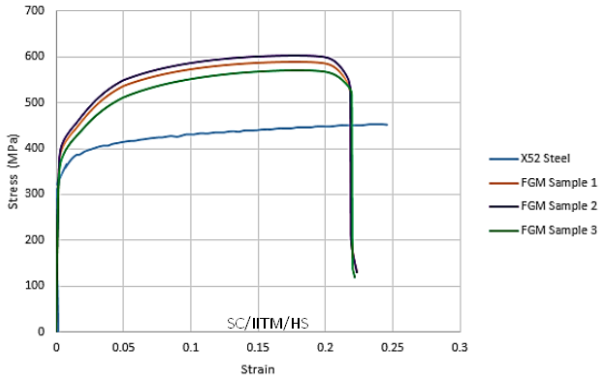

a) longitudinal direction

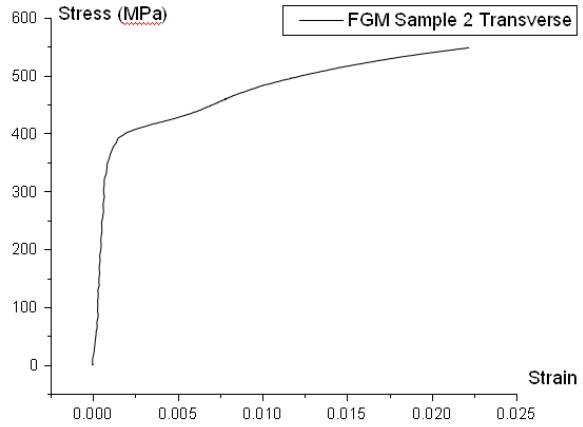

b) lateral direction

Figure 8. Stress-strain relationship of FGM

Table 2. Mechanical properties of FGM builds

Material/Parameters	X52Marine Riser Steel	FGM
Youngs Modulus (GPa)	210	209.66 ± 4.48
Yield Strength (MPa)	358	390.66 ± 12.23
Ultimate Strength (MPa)	453	587.66 ±12.76
Strength Ratio	1.265	1.50 ± 0.02
Ductility Ratio	32.207	45.47 ± 0.82
Tensile Toughness (J/m3)	104.92	120.50 ± 2.84
Poisson`s Ratio	0.3	0.30 ± 0.07
% Elongation	21	22.31± 0.11

Variation in micro-hardness along the build is assessed using the Vickers Hardness test. Figure 10 shows the result, which confirms that hardness is in the range of (307-320) at the interface. A pitting corrosion test showed about twelve times more corrosion in X52 steel than the proposed FGM.

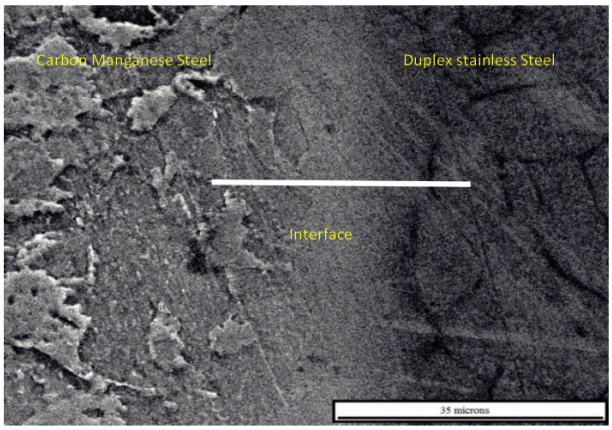

Figure 9. EDX image at the interface of FGM mould

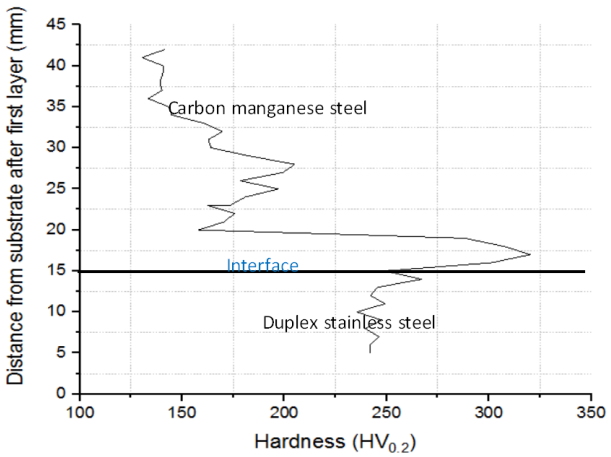

Figure 10. Micro-hardness variation in FGM build

3. Conclusions

Materials for the construction of marine structures should complement the form-dominance criteria and the strength and functional requirements to sustain the ocean environment hazards. While the design procedures are shifted to a form-centric approach, properties in materials need to be upgraded in parallel. The presented study illustrated the fabrication of FGM and its application to marine structures.More details can be seen in the detailed studies carried out by the authors [10,12]. It is seen that FGM possesses a higher yield and ultimate strength in comparison to the steel currently deployed for marine construction. In addition, it also offers excellent corrosion resistance, which was not satisfactory in the former. Significant enhancement in ductility guarantees its complementary support to large displacement characteristics of compliant marine structures. Rigorous studies on similar lines would suffice a stronger inclination for the design codes to recommend FGM as a structural material shortly.

References

[1] Chandrasekaran, S., Arvind Kr. Jain, Nasir Shafiq, M., et al., 2021. Design aids for offshore platforms under special loads, CRC press, Florida. pp. 280, ISBN: 9781032136844.

[2] Chandrasekaran, S., Nagavinothini, R., 2020, Offshore compliant platforms: Analysis, design and experimental studies, Wiley, U.K, ISBN: 978-1-119-66977-7.

[3] Chandrasekaran, S., 2019. Advanced steel design of structures, CRC press, Florida, ISBN: 978-036-72-3290-0.

[4] Chandrasekaran, S., 2020. Offshore Semi-Submersible Platform Engineering, CRC Press, Florida. pp. 240, ISBN: 978-0367673307.

[5] Chandrasekaran, S., Syed Azeem Uddin, 2020. Dynamic analysis of semi-submersible under postulated failure of restraining system with the buoy, Intl. J. of Steel Structures. 21(1), 118-131.

[6] DNV-RP-F205, 2010. Global Performance Analysis of Deepwater Floating Structures.

[7] Chandrasekaran, S., Nagavinothini, R., 2020. Parametric studies on the impact response of offshore triceratops in ultra-deep waters, Structure and Infrastructure Engineering. 16(7), 1002-1018.

[8] Chandrasekaran, S., Nagavinothini, R., 2020. Offshore triceratops under impact forces in ultra-deep arctic waters, Int. J. of Steel structures. 20(2), 464-479.

[9] Albino, J.C.R., Almeida, C.A., Menezes, I.F.M., et al., 2018. Co-rotational 3D beam element for nonlinear dynamic analysis of risers manufactured with functionally graded materials (FGM), Engineering Structures. 173, 283-299.

[10] Chandrasekaran, S., 2020. Design of Marine Risers with Functionally Graded Materials, Woodhead Publishing, Elsevier. pp. 200, ISBN: 978-0128235379.

[11] Chen, X., Li, J., Cheng, X., et al., 2017. Microstructure and mechanical properties of the austenitic stainless steel 316L fabricated by gas metal arc additive manufacturing, Mat. Sc. and Engg.,: A. 703, 567-577.

[12] Chandrasekaran, S., Hari, S., Murugaiyan, A., 2020. Wire arc additive manufacturing of functionally graded material for marine risers, J. Mat. Sc., & Engg. A. 792, 139530.

[13] Martina, F., Mehnen, J., Williams, S.W., et al., 2012. Investigation of the benefits of plasma deposition for the additive layer manufacture of Ti–6Al–4V, J. Mat.

Processing Tech. 212(6), 13.

[14] Shen, Y., Jukes, P., 2015. Technical challenges of unbonded flexible risers in HPHT and deep-water operations, Proc. of Twenty-fifth Int. Offshore and Polar Engg. Conf., June 21-26, Hawaii, USA.

[15] DNV, G., 2018. *DNVGL-RP-F112 Duplex Stainless Steel – Design against hydrogen-induced stress cracking*, DNV GL, 1-44.

[16] DNV, G., 2012. *DNV-OS-F101 Submarine pipeline systems*, Oslo: DNV GL, 1-367.

[17] Phifer, E.H., Kopp, F., Swanson, R.C., et al., 1994. Design and installation of auger steel catenary risers, Proc. of Offshore Technology Conference, 2-5 May, Houston.

NASS
NAN YANG ACADEMY OF SCIENCES

Tel:+65 65881289
E-mail:contact@nassg.org
Add:12 Eu Tong Sen Street #07-169 Singapore 059819

2661-3158 01
9 772661 315229